

**UNCLASSIFIED**



**Australian Government**  
**Department of Defence**  
Defence Science and  
Technology Organisation

# CTH Implementation of a Two-Phase Material Model With Strength: Application to Porous Materials

*A.D. Resnyansky*

**Weapons Systems Division**  
Defence Science and Technology Organisation

DSTO-TR-2728

## **ABSTRACT**

A material model accounting for strength developed earlier for two-phase materials is implemented in the CTH hydrocode. The strain response to load in the model is decoupled into shear and volumetric contributions in order to satisfy the model implementation requirements for CTH. Multi-phase description is realised via constitutive equations complementing the conservation laws for a material represented as a mixture of several phases. Such a formulation agrees well with the CTH code structure and is suitable for conventional user implementation. The implementation has been applied to a generic material representing sand at various porosities. The constitutive equations and equations of state have been fitted in order to describe literature data. Numerical illustrations in the report demonstrate agreement of the calculation results with the anomalous behaviour observed in the literature for a highly porous sand at shock compression and a good description of the experiments available in the literature on the explosion of a sand-buried charge.

## **RELEASE LIMITATION**

*Approved for public release*

**UNCLASSIFIED**

UNCLASSIFIED

*Published by*

*Weapons Systems Division  
DSTO Defence Science and Technology Organisation  
PO Box 1500  
Edinburgh South Australia 5111 Australia*

*Telephone: (08) 7389 5555  
Fax: (08) 7389 6567*

*© Commonwealth of Australia 2012  
AR-015-382  
July 2012*

**APPROVED FOR PUBLIC RELEASE**

UNCLASSIFIED

## UNCLASSIFIED

# CTH Implementation of a Two-Phase Material Model With Strength: Application to Porous Materials

## Executive Summary

Involvement of the Australian Defence Forces (ADF) in various operational theatres requires improvement of protective capability against buried mines and Improvised Explosive Devices (IEDs). The threat to a target (e.g., a vehicle) due to a detonating buried device is twofold: i) the structural threat due to mainly gaseous detonation products that are loading the target quite slowly in the millisecond range of time and over a wide area of the target; and ii) the impact threat due to the soil ejecta colliding with the target and transferring momentum to the target rather quickly within the microsecond range of time and localised over a compact area of the target. The impact threat is the most immediate and important one before the structural effects take place.

To develop a protection capability against this impact threat, an enhanced assessment of the response of porous geological materials blanketing a detonating device and transferring momentum to the target via the ejecta impact needs to be undertaken. Such an assessment can be performed with the physics modelling tools, hydrocodes, such as LS-DYNA and CTH available in DSTO. However, even with the use of these powerful modelling techniques, behaviour of the porous geological materials, commonly sand or soil, is not easy to describe in the conditions of shock loading. Complexity in the behaviour of porous materials, demonstrated for example in [1], is manifested by highly non-linear response of those materials due to their multi-phase structure with drastically different compressibilities of constituents. In turn, the solid constituents of these porous mixtures are strength resistant and strain rate sensitive. This behaviour, specifically evaluation of the parameters responsible for the momentum transfer, is not well predicted within the traditional approaches using established material models available in the hydrocodes.

In order to improve the hydrocode modelling capability, the present report describes an implementation of an advanced two-phase material model [2] that takes into account the multi-phase nature of the geological materials (sand, soil, etc). Along with the air contained in the pores, the condensed constituents of the materials are also compressible at this level of loads. In addition, the solid constituents are strength and strain rate sensitive. In the present report, the two-phase model [2] is implemented in the CTH hydrocode [3] and the implementation flowchart is briefly outlined. Sand is

## UNCLASSIFIED

## UNCLASSIFIED

considered as a model material in the test calculations. Mechanical characteristics of the material are fitted in order to correlate with available literature data for the constituents, namely, the air and quartz. The numerical illustrations demonstrate a good description of physical features that are typical for the porous materials at shock compression and are difficult to describe with material models available in the hydrocode. The first numerical example demonstrates the anomalous behaviour observed in experiments for highly porous sand, but this behaviour is not customarily predicted by available material models within the physics-modelling framework of the hydrocode. The second example illustrates formation of the soil ejecta due to explosion of a buried charge. Comparison of the numerical results with available literature experiments shows good agreement. The illustrations demonstrate the importance of the physics modelling for the description of parameters responsible for the momentum transfer from the soil ejecta to a target.

The present model development and CTH implementation activity is also performed as a part of the joint efforts within the Modelling and Simulation Focus Area of the Conventional Weapons Technology Group (Terminal Effects) of The Technical Cooperation Program (TTCP).

## References

- [1] Resnyansky A.D., Constitutive Modelling of Hugoniot for a Highly Porous Material, *J. of Appl. Physics*, 2008, v. 104, n. 9, pp. 093511-14.
- [2] Resnyansky A.D., Constitutive modeling of shock response of phase-transforming and porous materials with strength, *J. of Appl. Physics*, 2010, v. 108, n. 8, pp. 083534-13.
- [3] Bell R.L., Baer M.R., Brannon R.M., Crawford D.A., Elrick M.G., Hertel E.S. Jr., Schmitt R.G., Silling S.A., and Taylor P.A., *CTH user's manual and input instructions* version 7.1, Sandia National Laboratories, Albuquerque, NM, 2006.

## UNCLASSIFIED

UNCLASSIFIED

## Author

### **A. D. Resnyansky** Weapons Systems Division

*Anatoly Resnyansky obtained a MSc in Applied Mathematics and Mechanics from Novosibirsk State University (Russia) in 1979. In 1979-1995 he worked in the Lavrentyev Institute of Hydrodynamics (Russian Academy of Science) in the area of constitutive modelling for problems of high-velocity impact. Anatoly obtained a PhD in Physics and Mathematics from the Institute of Hydrodynamics in 1985. In 1996-1998 he worked in a private industry in Australia. He joined the Weapons Effects Group of the Weapons Systems Division (DSTO) in 1998. His current research interests include constitutive modelling and material characterisation at high strain rates, ballistic testing and simulation, and theoretical and experimental analysis of multi-phase flows. He has published over one hundred research papers.*

---

UNCLASSIFIED

UNCLASSIFIED

*This page is intentionally blank*

UNCLASSIFIED

## Contents

<b>1. INTRODUCTION.....</b>	<b>1</b>
<b>2. CONSTITUTIVE MODEL .....</b>	<b>3</b>
2.1 Conservation Laws and Constitutive Equations.....	3
2.2 Gibbs Energies and Thermodynamic Potentials of two-phase mixture .....	4
<b>3. CONSTITUTIVE RELATIONS AND EOS.....</b>	<b>6</b>
3.1 Equation of State of two-phase mixture .....	6
3.2 Constitutive Relations characterising strength .....	7
3.3 Thermo-Mechanical and Mass-Exchange constitutive relations .....	8
3.4 Compaction kinetic.....	9
<b>4. CTH IMPLEMENTATION.....</b>	<b>10</b>
4.1 Input Block.....	10
4.1.1 EOSVEI modifications .....	10
4.1.2 EOSVEK modifications.....	11
4.1.3 UINEP modifications .....	11
4.1.4 UINCHK modifications.....	12
4.1.5 UINISV modifications.....	13
4.2 Lagrangian Block .....	13
4.2.1 ELSG modifications.....	13
4.3 Eulerian Remap Block.....	14
4.3.1 EREB modifications.....	15
<b>5. SHOCK PROPAGATION IN HIGHLY POROUS MATERIAL.....</b>	<b>15</b>
5.1 Parameters and Hugoniot of Silica.....	16
5.2 Shock compression calculations using verified code .....	17
5.3 Shock compression calculations using the CTH implementation .....	20
5.4 Shock compression calculations using models available in CTH.....	23
<b>6. BURIED CHARGE MODELLING.....</b>	<b>25</b>
6.1 The problem statement .....	26
6.2 Calculations for Large Depth of Burial .....	29
6.3 Calculations for Small Depth of Burial .....	34
<b>7. CONCLUSIONS.....</b>	<b>42</b>
<b>ACKNOWLEDGEMENTS .....</b>	<b>43</b>
<b>REFERENCES .....</b>	<b>43</b>

UNCLASSIFIED

DSTO-TR-2728

*This page is intentionally blank*

UNCLASSIFIED

## 1. Introduction

Neutralisation of the effects of mines and buried Improvised Explosive Devices (IEDs) on affected vehicles and personnel requires an analysis of the target loading due to the explosion of a buried charge. Such an analysis involves a number of factors to consider. The most important ones amongst them are the size and area distribution of the charge, mechanical and thermal properties of the soil, the depth of burial, and the target stand-off distance. Other factors such as method of initiation, casing arrangement, and the properties of high explosive are still important, but they are somewhat secondary for charges buried under a layer of soil that is thick enough, as soon as the distribution of the energy to be released at a given depth of burial is known.

The most critical factor of the target loading analysis, the momentum transfer from the soil ejecta to a target such as a vehicle's floor, is mainly controlled by the density and velocity distributions through the ejecta thickness when the ejecta is impacting the target. The ejecta impact provides the highest level of the stress transfer contribution into the target, which may possibly be transmitted to the vehicle's occupants behind the floor barrier facing the ejecta. The follow-up blast products provide a comparably smooth and gradual loading, highly energetic, though, to affect the target's structural integrity and behaviour. Another important factor for the analysis is separation of the blast products from the soil particles (velocity non-equilibrium in the gas-solid mixture). This factor is negligible for the camouflet blasts (the detonation products are contained underground) when the Depth Of Burial (DOB) is sufficiently large or the products do not break the surface before the ejecta reaches the target. On the other hand, if 1) DOB is not sufficient or/and 2) the target stand-off distance is large, then the gaseous products may break through and the gas-particle separation may increase with time and distance of travel making this factor more influential. At the same time, the localised impact damage effects on the target due to the charge explosion diminish with increasing stand-off distance or/and decreasing DOB. Moreover, structural effects could possibly be analysed while neglecting the ejecta impact on the target when using, as a basis for the analysis, the residual energy of the blast products after having broken through the soil. Therefore, the scenarios when this non-equilibrium is significant are of less interest from the viewpoint of the localised damage effects to vehicle and vehicle occupants. When evaluating these effects, the mass-velocity distribution determining the momentum transfer is believed to be the more relevant ejecta-related factor. Thus, omitting the structural response issue, the present consideration is restricted to the velocity equilibrium case. In the two-phase analysis, synergistic effects might also be taken into account if the impact and blast loadings occur simultaneously.

For an analysis of behaviour of porous geological materials such as soil or sand we need to pay attention to a quite complex material response requiring an advanced approach. The first issue of the analysis is the porosity of the substances. The second issue is the complex behaviour of the solid constituents of the materials. Specifically, the silicon dioxide (silica) that is the most common component of the solid constituents of soils is known for by its abundance of high-temperature and high-pressure polymorphs. Other issues involve the presence of feldspar minerals and water (moisture content) that may easily change its phase state during the shock loading. As a starting point, we consider the two-phase representation of sand as a porous material with the solid silica constituent, omitting the phase transitions of

UNCLASSIFIED

DSTO-TR-2728

silica in the present consideration. Further work is planned to account for a phase transition using the three-phase modelling approach [1]. In the present work we employ a two-phase material model with strength [4].

Referring to the model implementation process, the user-implementation interface of modern hydrocodes poses certain restrictions on the implementation of material models in codes such as LS-DYNA [2] or CTH [3]. The two most critical restrictions are i) the use of the fundamental form of the conservation laws, namely, the mass, momentum, and energy conservation laws, and ii) the necessity of the decoupled representation of mechanical response in the form of separate spherical and deviatoric stress responses of a material. The decoupled response separates the pressure contribution calculations for the momentum update within the thermodynamic block of a code from the deviatoric stress calculations for the internal material parameters update within the constitutive block of the code. An example of an implementation dealing with these issues is shown in [5] for a rate sensitive strength model. Having specified the restrictions, it is still possible for code developers to implement, for example, a fully coupled system for the full deformation gradient or stress tensor (e.g. see the manual [3] for an example of the Transverse Isotropic (TI) model). The code developers can also escape the solitary form of the conservation laws and implement a few systems of the conservation laws for material components (e.g. see [3] for a few implementations of the Baer-Nunziato multi-phase flow model). However, such implementations require almost full access to the code and cannot be made via the user-implementation interface.

The initial version of the model being implemented in the present work has been published in [6]. Further development of this model has considered the inter-phase heat transfer, which is critical for porous materials and allowed the author to simulate the anomalous behaviour at shock compression [7]. The recent version [4] of the two-phase model has taken into account the strength resistance of condensed phases and, in turn, rate sensitivity of the yield limits of the phases. The present work deals with the CTH implementation of the two-phase model [4] that considers the inter-phase heat transfer and strength effects taking rate sensitivity into account. In this work, the CTH implementation is realised for two-phase porous materials. Adjustment of the implementation to any two-phase material, where phases are both condensed and the phase transition is possible, is a routine process provided that the phase transition kinetic is known (e.g. such an adjustment has been performed in an in-house wave code [4]).

When implementing the model in a hydrocode, the present model formalism, similarly to [5], allows one to decouple stress response in two processing streams: 1) Elasto-Plastic (EP) block processing Constitutive Equations (CE) that describe the evolution of deviatoric elastic deformations directly linked with the shear stresses; and 2) Eulerian Remap Block (ERB) processing thermodynamic relations on the basis of Equations Of State (EOSs) that describe the volumetric (bulk) response of materials. Strictly speaking, constitutive equations may be used for calculation of not only the deviatoric stress evolution, but other internal variables. Because of the code structure, the CE block is used at the code point when deviatoric stresses are calculated and this block can be used for any evolution equations. Therefore, references to the CE and EP blocks are interchangeable in this report.

The procedure of implementation in CTH is briefly described below with references to the code structure available in the public literature. The main CTH structure includes the Input

UNCLASSIFIED

Block (IB), Lagrangian Block (LB), and Eulerian Remap Block (ERB) [8]. An essential component of CTH is the Database Management Block (DMB) that arranges, allocates, stores, and retrieves the data. However, this block is not separated from the remaining blocks, likewise IB, LB, and ERB are separated from each other. Rather, DMB code fragments precede every call of any major subroutine from IB, and, particularly, LB and ERB blocks. This enables the user to ignore the CTH database structure, unless, like in the present case, the database management requires additional allocation due to extra requirements for internal state variables. Publications [9, 10] describe the code structure in slightly more detail with references to specific routines of the code. The present implementation includes modifications to i) the input subroutines of the EP module in the IB part, ii) update of deviatoric stresses and extra variables in the LB part; and iii) update of key thermodynamic variables and extra variables using advected parameters and EOS in the ERB part. A recent CTH implementation in DSTO [5] describes the basic steps of the implementation. However, the present model is essentially more complex than that of [5] and requires more extensive use of extra variables and EOS modules of CTH.

To illustrate numerically the present implementation, a response of generic sand is modelled with constituents of quartz and air. The model uses known thermo-mechanical data for polycrystalline or fused quartz with the air described as a polytropic gas. Numerical examples include the simulation of the shock wave compression of a highly porous sand, and the calculation results are compared with the shock compression data for silica [11]. With this calculation, the CTH code employing the present implementation demonstrates its ability to describe the anomalous behaviour of the Hugoniots [11] at a high porosity. Another example is the simulation of the expansion of an initiated High Explosive (HE) charge buried under a layer of sand. The experiments [12] are compared with the CTH calculations using two CTH database models and the implemented model. The numerical results show that the present model demonstrates an improvement in predictions when comparing with the models available in CTH.

## 2. Constitutive Model

### 2.1 Conservation Laws and Constitutive Equations

The system of equations of the two-phase model with strength contains three conservation laws for mass, momentum and total energy with the stress tensor in the decoupled form  $\sigma_{ij} = s_{ij} - p\delta_{ij}$  (see [4]):

$$\begin{aligned} \frac{\partial \rho}{\partial t} + \frac{\partial \rho u_k}{\partial x_k} &= 0, \quad \frac{\partial \rho u_i}{\partial t} + \frac{\partial (\rho u_i u_j - s_{ij})}{\partial x_j} + \frac{\partial p}{\partial x_i} = 0, \\ \frac{\partial \rho \left( e + \frac{u^2}{2} \right)}{\partial t} + \frac{\partial \left[ \rho u_j \left( e + \frac{u^2}{2} \right) - s_{ij} u_i + p u_j \right]}{\partial x_j} &= 0. \end{aligned} \quad (1)$$

Denotations of the physical variables are standard and described in [4]. The strength response is described by 'specific' strain  $e_{ij}$  when small shear deformations are assumed (see [1, 4, 5]).

## UNCLASSIFIED

DSTO-TR-2728

Description of the strength response uses the same symmetrical velocity gradient as the majority of other strength sensitive models in CTH. The response is described by the following system of equations [4]:

$$\frac{\partial \rho e_{ij}}{\partial t} + \frac{\partial \rho e_{ij} u_k}{\partial x_k} - \frac{\partial u_i/2}{\partial x_j} - \frac{\partial u_j/2}{\partial x_i} + \frac{\partial u_k/3}{\partial x_k} \cdot \delta_{ij} = -(\theta \varphi_{ij}^{(1)} + (1-\theta) \varphi_{ij}^{(2)}) - \rho \lambda_{ij} \psi, \quad (2)$$

where  $\varphi_{ij}^{(1)} = \rho [e_{ij} + (1-\theta) \lambda_{ij}] / \tau_1$  and  $\varphi_{ij}^{(2)} = \rho [e_{ij} - \theta \lambda_{ij}] / \tau_2$ . Superscript indices refer to the material constituent number and  $\tau_1$  and  $\tau_2$  are the relaxation time functions obtained for rate sensitive materials of the phases from the corresponding yield limits versus strain rate (see [13]). The parameters  $c$  and  $\theta$  are mass and volumetric concentrations of the first phase and  $\lambda_{ij}$  are components of the strain inter-phase imbalance [4], which evolves in accordance with the following constitutive equation [4]:

$$\frac{\partial \rho \lambda_{ij}}{\partial t} + \frac{\partial \rho \lambda_{ij} u_k}{\partial x_k} = -(\varphi_{ij}^{(1)} - \varphi_{ij}^{(2)}). \quad (3)$$

Function  $\psi$  in the last term of the right-hand side of the equations (2) is the compression kinetic from the following constitutive equations describing the phase transition and compaction due to relative compressibility between the phases [4]:

$$\frac{\partial \rho c}{\partial t} + \frac{\partial \rho c u_j}{\partial x_j} = -\rho \varphi = m_0, \quad \frac{\partial \rho \theta}{\partial t} + \frac{\partial \rho \theta u_j}{\partial x_j} = -\rho \psi. \quad (4)$$

The inter-phase heat transfer is described with the following equation for the entropy disequilibrium  $\chi$  [4]:

$$\frac{\partial \rho \chi}{\partial t} + \frac{\partial \rho \chi u}{\partial x} = -\rho \omega. \quad (5)$$

The inter-phase heat exchange kinetic  $\omega$  is also to be specified [4, 7].

The system of differential equations of this subsection describes the behaviour of a two-phase mixture. However, this system calculates only the evolution of independent thermodynamic and kinematic variables (with the exception of entropy described indirectly by the energy conservation law). Therefore, the system should be completed with algebraic equations for dependent thermodynamic variables, which includes the kinetic functions for the constitutive equations and an equation of state.

## 2.2 Gibbs Energies and Thermodynamic Potentials of two-phase mixture

In order to specify relations between the dependent variables  $e$ ,  $p$ ,  $s_{ij}$ , and  $T$  and independent variables  $\rho$ ,  $c$ ,  $\theta$ ,  $S$ ,  $e_{ij}$ ,  $\lambda_{ij}$ , and  $\chi$ , we need to recall the relations between the averaged variables and the variables associated with individual phases [4]. The phase-specific variables are

UNCLASSIFIED

marked by superscripts '1' and '2' in parentheses for the first and second phases, respectively, with the first phase being air in the case of a porous material. Specifically, the phase independent variables are calculated from the averaged variables, using the concentration and disequilibrium parameters from the following relations [4]:

$$\begin{aligned} \rho^{(1)} &= \rho c / \theta, \quad \rho^{(2)} = \rho(1 - c) / (1 - \theta), \quad S^{(1)} = \frac{1}{2}(S + \chi) / c, \quad S^{(2)} = \frac{1}{2}(S - \chi) / (1 - c), \\ e_{ij}^{(1)} &= \theta (e_{ij} + \lambda_{ij} (1 - \theta)) / c, \quad e_{ij}^{(2)} = (1 - \theta) (e_{ij} - \lambda_{ij} \theta) / (1 - c). \end{aligned} \quad (6)$$

The dependent averaged variables are calculated via the phase ones as follows

$$\begin{aligned} e &= c e^{(1)} + (1 - c) e^{(2)}, \quad p = \rho^2 e_\rho = \theta p^{(1)} + (1 - \theta) p^{(2)}, \quad T = e_S = (T^{(1)} + T^{(2)})/2. \\ s_{ij} &= e_{e_{ji}} = (ce^{(1)} + (1 - c)e^{(2)})_{e_{ji}} = \theta s_{ij}^{(1)} + (1 - \theta)s_{ij}^{(2)}. \end{aligned} \quad (7)$$

The fundamental thermodynamic characteristics used for the description of the mixture equilibrium is the Gibbs energy for each phase  $\mu_k = e^{(k)} + p^{(k)} / \rho^{(k)} - T^{(k)} S^{(k)} - e_{ij}^{(k)} s_{ij}^{(k)}$ ,  $k = 1, 2$ . Affinity of the Gibbs energies characterizes phase stability (see [1] for details and an example). Similar generalization of the Gibbs energy for specific materials has been considered earlier for two-phase mixtures without strength in [6, 14] and for the mixtures with strength in [1, 4, 5]. Using the Gibbs energy, the thermodynamic potentials of the mixture are (see [4] for details)

$$\begin{aligned} \Lambda &= e_c = e^{(1)} + \frac{p^{(1)}}{\rho^{(1)}} - T^{(1)} S^{(1)} - e_{ij}^{(1)} s_{ij}^{(1)} - e^{(2)} - \frac{p^{(2)}}{\rho^{(2)}} + T^{(2)} S^{(2)} + e_{ij}^{(2)} s_{ij}^{(2)} = \mu_1 - \mu_2, \\ Q_{ij} &= e_{\lambda_{ji}} = \theta (s_{ij}^{(1)} - s_{ij}^{(2)}), \\ \Pi &= e_\theta = -\frac{p^{(1)} - p^{(2)}}{\rho} + \frac{s_{ij}^{(1)} (\rho^{(1)} e_{ij}^{(1)}) - s_{ij}^{(2)} (\rho^{(2)} e_{ij}^{(2)})}{\rho} - \lambda_{ij} s_{ij} = \Pi_0 - \lambda_{ij} s = \\ &= -\frac{p^{(1)} + (\rho^{(1)} e_{ij}^{(1)}) (s_{ij}^{(1)} - s_{ij}) - p^{(2)} - (\rho^{(2)} e_{ij}^{(2)}) (s_{ij}^{(2)} - s_{ij})}{\rho}, \\ \Psi &= e_\chi = (T^{(1)} - T^{(2)})/2. \end{aligned} \quad (8)$$

In order to satisfy thermodynamic correctness, the constitutive relations have the following restrictions on the right-hand sides (see [4]):

$$\varphi = \Lambda \cdot \varphi_0, \quad \psi = \Pi_0 \cdot \psi_0, \quad \omega = \Psi \cdot \omega_0. \quad (9)$$

Thus, when equations of state are given for each phase in the form

$$e^{(1)} = e^{(1)}(\rho^{(1)}, e_{ij}^{(1)}, s^{(1)}), \quad e^{(2)} = e^{(2)}(\rho^{(2)}, e_{ij}^{(2)}, s^{(2)}), \quad (10)$$

the conservation laws (1) and the constitutive equations (2)-(5) generate a closed system of equations. The system can be solved numerically if functions  $e^{(1)}$ ,  $e^{(2)}$  and  $\varphi_0$ ,  $\psi_0$ ,  $\omega_0$  are

## UNCLASSIFIED

DSTO-TR-2728

specified. An example of such a specification for porous sand will be shown in the next Section.

### 3. Constitutive Relations and EOS

#### 3.1 Equation of State of two-phase mixture

For porous materials, we specify the first phase to be air and the second phase a solid constituent. In the present implementation, to determine EOS (10) for the condensed constituent (the second phase in a porous mixture denoted by superscript '2'), we choose a reduced form of the Mie-Grüneisen-type EOS developed in [15] and used in [1, 4- 7]:

$$e(\rho, e_{ij}, S) = \frac{a_0^2}{2\alpha_0^2} \cdot (\delta^{\alpha_0} - 1)^2 + 2\rho_0^2 b_0^2 \delta^{\beta_0+2} d + c_{vs} T_0 \delta^{\gamma_0} \left[ \exp\left(\frac{S}{c_{vs}}\right) - 1 \right] + \frac{p_0}{\rho_0} - \frac{p_0}{\rho} . \quad (11)$$

Here,  $a_0$ ,  $\beta_0$ , and  $\gamma_0$  (Grüneisen coefficient) are material constants,  $c_{vs}$  is the thermal capacity, and  $\delta = \rho/\rho_{0S}$  with initial density  $\rho_{0S}$ . The constant  $a_0$  is the bulk sound velocity that is linked with the longitudinal and shear sound velocities  $d_0$  and  $b_0$  as follows

$$a_0^2 = d_0^2 - 4b_0^2/3 , \quad (12)$$

and  $d$  in (11) is the second invariant of the 'specific' strain deviator:  $d = e_{ij} \cdot e_{ji} / 2$ . It should be noted that the arguments and the function itself for the internal energy (11) refer only to the second constituent of the two-phase mixture.

Shear stresses are calculated from (11) for the solid phase as

$$s_{ij} = e_{e_{ij}} = e_d d_{e_{ij}} = e_d e_{ij} = 2\rho_0^2 b_0^2 \delta^{\beta_0+2} e_{ij} = 2\rho b_0^2 \delta^{\beta_0} \rho e_{ij} = 2G\rho e_{ij} . \quad (13)$$

Where the shear modulus  $G$ :  $G = \rho b_0^2 \delta^{\beta_0}$ .

For the first constituent in porous material, the air, EOS in (10) is selected in the ideal gas form:

$$e(\rho, e_{ij}, S) = \frac{c_0^2}{\gamma(\gamma+1)} \cdot (\delta^\gamma - 1) + c_{vg} T_0 \delta^\gamma \left[ \exp\left(\frac{S}{c_{vg}}\right) - 1 \right] . \quad (14)$$

Here  $\gamma$  is the polytropic gas exponent,  $c_0$  is the sound velocity,  $c_{vg}$  is the thermal capacity of the gas, and  $\delta = \rho/\rho_{0g}$  with the initial density  $\rho_{0g}$ . The following natural restriction follows from the definition of the ideal gas EOS:  $c_0^2 = \gamma(\gamma+1) c_{vg} T_0$ . In this case, the variables relate only to the phase '1'. The initial densities of the two constituents  $\rho_{0g}$  and  $\rho_{0S}$  are used along with the initial density of porous material  $\rho_0$  in order to define initial mass and volumetric

UNCLASSIFIED

concentrations  $c$  and  $\theta$  from (6). These concentrations and density are used as initial data for the system of conservation laws and evolution equations.

### 3.2 Constitutive Relations characterising strength

The accounting for the strength of the second constituent (in the case of porous material) is realised via the constitutive equations (2). In order to close the equations, the relaxation time functions for solid constituents with strength should be chosen. In the present case, the function for the second constituent is chosen in the following form [5, 13]:

$$\tau(\rho, s, T) = \tau_0 \frac{\exp\left[\frac{(D_0 + H\epsilon)/s}{N_0 + M\epsilon}\right]}{N_0 + M\epsilon} , \quad (15)$$

where  $s$  determined from  $s^2 = s_{ij} s_{ij}$  is the second invariant of the stress deviator. In the present work as well as in [13], the variable  $\epsilon$  is associated with the elastic portion of deformation  $\epsilon = s/(2G)$  and  $\tau_0, D_0, H, N_0, M$  are material constants. It should be noted that the constants in (11), (14) and (15) are specific to each phase and in the present implementation the function (15) is relevant only to the second phase of porous mixture. Thus, using the function (15) for the second phase as  $\tau_2$ , we can determine  $\varphi_{ij}^{(2)}$  and, assuming absence of any strength effects in the first gaseous phase, we take  $\varphi_{ij}^{(1)} = 0$  in (2) and (3) for the present case.

In order to facilitate choice of constants in (15), an algorithm of fitting the constants suggested in [13] has been realised in the present implementation. Let us briefly outline the algorithm. Firstly, the user has to select two yield limit points  $Y_1$  and  $Y_2$  at different strain rates  $\dot{\epsilon}_1$  and  $\dot{\epsilon}_2$ . It should be noted that this choice is a responsibility of the user and the present fit does not guarantee a proximity of any pre-determined experimental or hypothetical curve passing through the two given points in the  $(Y - \dot{\epsilon})$  plane to the curve obtained with this fit except for the two points specified. Secondly, the user needs to select constants  $N_0$  and  $M$  as an initial density and a multiplication factor of defects in the condensed material. As shown in [16], these constants have a much smaller influence on the fit of the curve than the constants  $\tau_0$  and  $D_0$ . The parameter  $H$  is tabulated for future use to describe the hardening behaviour of materials and cannot be used for modelling such a behaviour with the present choice of  $\epsilon$  in (15) (see discussion on this topic in [5]). Therefore, it is taken  $H = 0$  in the present case. The idea of fitting constants  $\tau_0$  and  $D_0$  in [13] is based on an approximation of the stationary solution of the viscoelastic model equations [17]. It was observed in [13] that this solution is sufficiently close to the yield limit point. The corresponding stress relaxation equations for characterising the plasticity state (a single-phase analogue of the equation (2)) are as follows (see [5]):

$$\frac{d\epsilon_{ij}^e}{dt} - \frac{1}{2} \left( \frac{\partial u_i}{\partial x_j} + \frac{\partial u_j}{\partial x_i} \right) = -\frac{\epsilon_{ij}^e}{\tau} . \quad (16)$$

## UNCLASSIFIED

DSTO-TR-2728

In the uniaxial stress conditions ( $\sigma_{22} = 0$ ), the yield limit is  $Y = \sigma_{11}$  and  $\dot{\varepsilon} = \partial u_1 / \partial x_1$ . Therefore, the stationary point of (16) after index summation can be found from

$$2G\dot{\varepsilon} = \frac{Y}{\tau}.$$

The last equation with  $\tau$  substituted by (15) results in

$$\ln \dot{\varepsilon} = \ln \frac{Y}{2G} - \ln \frac{\tau_0}{N_0} - \frac{D_0}{Y} \sqrt{\frac{3}{2}} + \ln \left( 1 + \frac{M}{2N_0} \frac{Y}{2G} \right), \quad (17)$$

that allows one to find  $\tau_0$  and  $D_0$  when two pairs  $\{Y_1, \dot{\varepsilon}_1\}$  and  $\{Y_2, \dot{\varepsilon}_2\}$  are given. Usually, these data are known from the Split Hopkinson Pressure Bar (SHPB) tests at compression. However, the same algorithm can be used for the tensile tests as well. For simplicity, we assume that when necessary we can utilize another pair at tension with yield limits  $Y_{1t}$  and  $Y_{2t}$  using the same strain rates. In the present implementation we use  $p < 0$  as a condition for use of the tensile yield limits.

### 3.3 Thermo-Mechanical and Mass-Exchange constitutive relations

Closure of the constitutive equation (5) describing inter-phase heat exchange can be done via specification of the right-hand side  $\omega$  for the equation. In conjunction with the thermodynamics condition (9), the required inter-phase heat exchange kinetic  $\omega_0$  in (5), (9) is used in the following form [4]

$$\omega_0 = 2\omega_0 \frac{h}{\rho} \frac{T^{(1)} + T^{(2)}}{T^{(1)}T^{(2)}}, \quad h = A_S \frac{k_{eff}}{d_0^2}, \quad k_{eff} = \frac{k_1 k_2}{k_2 \theta + k_1 (1 - \theta)}, \quad (18)$$

where  $h$  is the heat transfer coefficient,  $d_0$  is a typical material structure size (e.g. the grain or cell size for porous materials),  $A_S$  is a dimensionless coefficient (a function of the factors promoting or resisting the heat exchange, see [7] for details; in the present work  $A_S = 400$ ), and  $k_1$  and  $k_2$  are the thermal conductivities of the phases. Initial entropy concentration  $\chi$  can be calculated from initial temperatures  $T^{(1)} = \partial e^{(1)} / \partial s^{(1)}$ ,  $T^{(2)} = \partial e^{(2)} / \partial s^{(2)}$  and from densities (6) if the temperatures initially are not in equilibrium. Omitting this rather exotic case in the present implementation, we take  $s = 0$  and  $\chi = 0$  as the initial data (the initial temperatures of the phases take the reference values in this case).

For closure of the mass exchange constitutive equation (the first equation from the pair (4)), the function  $\varphi$  should be defined via the specification of  $\varphi_0$  from (9). In the case of a phase transition occurring between two phases of a two-phase material, an example of the definition of this function can be found in [4]. In the present case of a porous material, absence of the inter-phase mass exchange can be assumed. Therefore, the choice  $\varphi = 0$  in (20) for the porous mixture finalises definition of the mass-exchange kinetic.

## UNCLASSIFIED

### 3.4 Compaction kinetic

The last equation to be specified is the right-hand side  $\psi$  for the constitutive equation describing the inter-phase compressibility (the second equation from pair (4)). This function (the compaction kinetic) is normally determined from the SHPB compaction tests when the porous sample is confined within an assembly maintaining a constant pressure (e.g. see [18]) or within a container with rigid walls maintaining zero lateral strain. In the assumption of uniaxial strain, one-dimensional homogeneous deformation ( $u = \dot{\varepsilon} x + u_0$ ), and absence of mass exchange, the system of equations for determination of the compaction kinetic is reduced from (1-5) to the following

$$\begin{aligned} \frac{d \ln \rho}{dt} + \dot{\varepsilon} = 0, \quad \frac{de_{11}}{dt} - \frac{2}{3\rho} \dot{\varepsilon} = -\frac{(1-\theta)\varphi_{11}^{(2)}}{\rho} - \lambda_{11}\psi, \quad \frac{d\lambda_{11}}{dt} = \frac{\varphi_{11}^{(2)}}{\rho}, \\ \frac{de_{22}}{dt} + \frac{1}{3\rho} \dot{\varepsilon} = -\frac{(1-\theta)\varphi_{22}^{(2)}}{\rho} - \lambda_{22}\psi, \quad \frac{d\lambda_{22}}{dt} = \frac{\varphi_{22}^{(2)}}{\rho}, \\ \frac{d\theta}{dt} = -\psi, \quad \frac{d\chi}{dt} = -\omega, \quad \frac{dS}{dt} = \Phi. \end{aligned} \quad (19)$$

Here,  $\dot{\varepsilon}$  is the rate of deformation, which can be a function of time, and the entropy dissipation term in (19) is (see [4]):

$$\Phi = \frac{1}{T} \left[ \varphi \Lambda + \psi \Pi_0 + \omega \Psi + \frac{\theta \varphi_{ij}^{(1)} s_{ij}^{(1)} + (1-\theta)\varphi_{ij}^{(2)} s_{ij}^{(2)}}{\rho} \right]. \quad (20)$$

In the absence of inter-phase mass exchange for the present case,  $\varphi = 0$  and, because of the gaseous first phase,  $\varphi_{ij}^{(1)} = 0$ . Keeping in mind that the relaxation function  $\tau_2$  is assumed to be determined from appropriate SHPB data for the second constituent, we can rewrite (19) in the following further reduced form

$$\begin{aligned} \frac{d \ln \rho}{dt} + \dot{\varepsilon} = 0, \quad \frac{ds_{11}^{(2)}}{dt} = \frac{2}{3} 2G_2 \dot{\varepsilon} - \frac{s_{11}^{(2)}}{\tau_2}, \quad \frac{ds_{22}^{(2)}}{dt} = -\frac{1}{3} 2G_2 \dot{\varepsilon} - \frac{s_{22}^{(2)}}{\tau_2}, \\ \frac{d\theta}{dt} = -\psi, \quad \frac{d\chi}{dt} = -\omega, \quad \frac{dS}{dt} = \Phi, \quad \Phi = \frac{1}{T} \left( \psi \Pi_0 + \omega \Psi + \frac{(1-\theta)\varphi_{ij}^{(2)}}{\rho} s_{ij}^{(2)} \right), \end{aligned} \quad (21)$$

where  $s_{ij}^{(2)} = 2G_2(e_{ij} - \lambda_{ij}\theta)$ . Therefore,  $\rho\lambda_{ij} = -s_{ij}^{(2)}/2G_2$ , and  $\rho e_{ij} = (1-\theta)s_{ij}^{(2)}/2G_2$ . The system (21) for the stress tensor has been obtained from (19), when multiplying the corresponding equations by  $G_2$  (assuming this modulus to be a constant within a single time step) and by manipulation of the 'specific' strain and the strain disbalance to produce  $s_{ij}^{(2)}$ . Thus, the system (21) allows one to calculate  $\rho$ ,  $\theta$ ,  $\chi$ ,  $S$ ,  $e_{11}$ ,  $e_{22}$ ,  $\lambda_{11}$ , and  $\lambda_{22}$  as soon as the right hand sides in (21) are given. Here  $c$  is constant due to the absence of mass exchange in the porous mixture. The stresses  $\sigma_{ij} = s_{ij} - p\delta_{ij}$  are computed from (7) as follows

$$\sigma_{11} = (1-\theta)s_{11}^{(2)} - \theta p^{(1)} + (1-\theta)p^{(2)}, \quad \sigma_{22} = (1-\theta)s_{22}^{(2)} - \theta p^{(1)} + (1-\theta)p^{(2)}, \quad (22)$$

## UNCLASSIFIED

DSTO-TR-2728

where  $p^{(1)}$  and  $p^{(2)}$  are obtained from EOSs (14) and (11), using the thermodynamic identity for individual phases, similarly to (7). Summarizing, while the functions  $\tau_2$  and  $\omega$  having been pre-determined, the function  $\psi$  can be fitted from the stress-strain curves recorded during SHPB compaction experiments.

As a first approximation case for the compaction kinetic of sand, the function  $\psi_0$  in (9) was taken from [6] in the following form:

$$\begin{aligned}\psi_0 &= \psi_{00}\theta (1-\theta) (\theta - \theta_0(p)) , \quad \text{at } \theta > \theta_0(p) , \\ \psi_0 &= 0 \quad , \quad \text{otherwise,}\end{aligned}\tag{23}$$

where  $\theta_0(p)$  is arranged in such a way that  $\theta_0 = \theta_{00}$  at  $p < p_c$  and  $\theta_0$  quickly drops from the initial value  $\theta_{00}$  to zero in a smooth way when  $p$  exceeds  $p_c$  (a simple polynomial approximation with the power exponent  $n_c$ ). This function (23) is used in the present calculations as a compaction kinetic.

## 4. CTH Implementation

The present implementation affects the CTH blocks, IB, LB, and ERB, mentioned earlier, and allocates extra memory in a DMB module of LB for the Internal State Variables (ISVs).

### 4.1 Input Block

For the input block, IB, three subroutines [5, 9, 10, 19], UINEP.FOR, UINISV.FOR, and UINCHK.FOR, are modified. In addition, modifications of two substitute subroutines, EOSVEI and EOSVEK, of the EOS input module are introduced in two subsequent subsections as described below.

#### 4.1.1 EOSVEI modifications

In order to conduct the EOS calculations, the substitute subroutines available for an EOS one-component VE model are replaced by subroutines representing the present EOS combined from (11) and (14) via the mixture rule (7). Thus, the 'VE' identifier along with the corresponding input data refers to the present EOS model. The input EOS data are taken from the EOS\_data array by selection of the material's name in the corresponding section related to the specified model. However, this dataset has to be replaced by explicitly given data that are necessary for the present model. In doing so, any material name can be used as the dummy name in the EOS input (for example, the material name 'pmma' is used in the input decks below).

The EOS subroutines require the initial densities of the mixture and phases (they are calculated later on in the EP part of the input). Thus, the initial density of the porous material

UNCLASSIFIED

and the densities of the first and second phases have to be calculated beforehand and introduced explicitly via three successive variables that are an input in the original VE subroutine (they are denoted by 'RO', 'T0' and 'CV', respectively, by the subroutine convention).

#### 4.1.2 EOSVEK modifications

The extra variables to be used in the EOS block are introduced in this subroutine because the EOS substitute subroutines do not provide access to the extra variables defined in the CE block. Thus, the value exchange between the EOS and CE extra variables at a common point of the code is needed (see subsection 4.3.1 below). The extra variables required by the EOS thermodynamics block for use with the model are: i) symmetric 'specific' strain 5-set tensor  $e_{ij}$  (ER variables); ii) scalar mass concentration  $c$  (CRMS variable); iii) scalar volume concentration  $\theta$  (RTET variable); iv) scalar entropy disequilibrium  $\chi$  (XIR variable); and v) symmetric strain disbalance 5-set tensor  $\lambda_{ij}$  (LMR variables). Specification of the internal parameters for each of the variables is described in more detail below, when outlining modifications for the subroutine UINISV. Along with the thermodynamic variables provided by CTH, this set is sufficient for calculation of all necessary thermodynamic functions in the EOS module.

#### 4.1.3 UINEP modifications

UINEP.FOR modifications read in the data from VP\_data input file into the VPUINP array allocated for the EP related input data [5, 19]. Because of the access restrictions to the EOS user-implementation block, both, EOS and CE data, are taken from the VP\_data input file that results in a fairly significant block of data. The data needed for the model input are: 'RHO', 'C0G', 'GAMG', 'RHOS', 'C0S', 'B0S', 'ALF', 'BET', 'GAMS', 'CVS', 'PRS0', 'LGEP1', 'LGEP2', 'Y1C', 'Y2C', 'Y1T', 'Y2T', 'AN2', 'AM2', 'TET00', 'PCR', 'ANCR', 'PSI00', 'D0', 'AKG', 'AKS', and 'AHTS'.

These constants represent the following:

- initial density of porous material for RHO ( $\rho_0$ );
- the bulk sound velocity of the gaseous phase for C0G ( $c_0$  in (14));
- the polytropic gas exponent for GAMG ( $\gamma$  in (14));
- initial density of the solid phase for RHOS ( $\rho_{0s}$  in (11))
- the bulk sound velocity of the solid phase for C0S ( $a_0$  in (11));
- the shear sound velocity of the solid phase for B0S ( $b_0$  in (11));
- the bulk modulus exponent of the solid phase for ALF ( $a_0$  in (11));
- the shear modulus exponent of the solid phase for BET ( $\beta_0$  in (11));
- the Grüneisen coefficient of the solid phase for GAMS ( $\gamma_0$  in (11));
- the thermal capacity of the solid phase for CVS ( $c_{vs}$  in (11));
- ambient pressure for PRS0 ( $p_0$  in (11));
- decimal logarithm of strain rate related to the first test point for LGEP1 ( $\log \dot{\epsilon}_1$  in (18));
- decimal logarithm of strain rate related to the second point for LGEP2 ( $\log \dot{\epsilon}_2$  in (18));
- the yield limit at compression related to the first point for Y1C ( $Y_1$  in (18));
- the yield limit at compression related to the second point for Y2C ( $Y_2$  in (18));
- the yield limit at tension related to the first point for Y1T ( $Y_{1t}$  in (18));

## UNCLASSIFIED

DSTO-TR-2728

- the yield limit at tension related to the second point for Y2T ( $Y_{2t}$  in (18));
- the initial defect density related to the solid phase for AN2 ( $N_0$  in(15));
- the defect multiplication coefficient related to the solid phase for AM2 ( $M$  in(15));
- the starting volume concentration for TET00 ( $\theta_{00}$  in (23));
- the critical pressure of the compaction kinetic for PCR ( $p_c$  in (23));
- the power exponent of polynomial approximation of the kinetic for ANCR ( $n_c$  in (23));
- the proportionality constant of the compaction kinetic for PSI00 ( $\psi_{00}$  in (23));
- the characteristic material structure size in the heat transfer kinetic for D0 ( $d_0$  in (18));
- the thermal conductivity of the gaseous phase for AKG ( $k_1$  in(18));
- the thermal conductivity of the solid phase for AKS ( $k_2$  in(18)); and
- the dimensionless coefficient of the heat exchange kinetic for AHTS ( $A_s$  in (18)).

It should be noted that the model uses non-standard input units in  $cm$  (length),  $g$  (mass),  $10\mu\text{sec} = 10^{-5}\text{sec}$  (time), and  $^\circ\text{K}$  (temperature). The strain rate  $\dot{\varepsilon}$  for LGEP1 and LGEP2 is taken in inverse seconds. If the value Y1T is negative then the data Y1T and Y2T are taken to be identical to the set Y1C and Y2C. The derived pressure unit in this dataset is GPa. At the end of the modifications, the initial value of Poisson's ratio, and the bulk and shear modulus are calculated and initially checked in the same UINEP.FOR subroutine.

#### 4.1.4 UINCHK modifications

UINCHK.FOR modifications call new subroutines VERCHK.FOR and VERCHX.FOR. Before the calls, the modified code checks if the assigned MODLEP number for the present constitutive model is in agreement with the substituted EOS number MEQ [19]. The next part of the modifications assigns the necessary model-type attributes of the model such that deviatoric stresses will be calculated. Then, a standard call to the subroutine SI2CTH introduces the unit transformation constants into a part of the input array VPUINP. The new subroutine VERCHK.FOR transforms the constants into the CTH units from the non-standard input units, introduces global constants (the 'GC' part [19] of the array VPUINP) such as the ambient pressure and reference temperature used in (11) and fills in the 'DC' part of the array with several derived constants used for EOS and CE calculations such as the time relaxation constants for (15).

The new subroutine VERCHX.FOR called afterwards replaces the EOS input data (UI) by the data from the VP\_data file, and recalculates auxiliary constants for the initial cycle of the EOS calculations (before the EP input) filling in the tail of the UI array for the EOS block [19] with these constants. The EOS constants previously taken from the EOS analogue of the VP\_data file are now replaced by the data described above in the present section, which is done when calling VERCHX.FOR. The whole set of variables, when comparing with only 3 variables introduced in EOSVEI.FOR, is prepared for the EOS module in this subroutine. However, the mass calculation is processed earlier than the elasto-plastic input and should be preceded by input of the EOS data. As mentioned in subsection 4.1.1, the code uses the EOS data for the initial cycle calculation of mass arrays. In order to use the input data correctly, when using the EOS identifier in the EOS section of the CTH input, we explicitly assign values of the initial mixture and phase densities for the EOS model to be substituted, while leaving the remaining parameters of the EOS input intact. These values should be in agreement with the value of 'RHO' in the VP\_data input, and with the values for the density of the gaseous phase calculated from C0G, GAMG and PRS0 and for density RHOS for the solid constituent.

## UNCLASSIFIED

#### 4.1.5 UINISV modifications

UINISV.FOR modifications make two calls for a standard subroutine MIGSEX [19] setting up default values for extra variables and for a new subroutine VEREXV. The subroutine VEREXV sets up extra variables to be used in the CE block. Some values of the extra variables are shared via the VERSWP subroutine outlined below in the ERB modifications. This value exchange is needed in the present implementation because access to the EOS block is limited and extra variables defined in EOSVEK above cannot be easily reached. The whole set of extra variables, which is required by both the CE and the EOS thermodynamics blocks for use with the model and being specified in the VEREXV subroutine, is: i) symmetric ‘specific’ strain 5-set tensor  $e_{ij}$  (E variables); ii) scalar mass concentration  $c$  (CMS variable); iii) scalar volume concentration  $\theta$  (TET variable); iv) scalar entropy disequilibrium  $\chi$  (XI variable); v) symmetric strain disbalance 5-set tensor  $\lambda_{ij}$  (LM variables); vi) the old density at the start of the time cycle calculation (RHOO variable); and vi) entropy at the start of the time cycle calculation (ENT variable). This set is sufficient to calculate all the necessary thermodynamic functions in both the EP and EOS modules. The tensor character for variables E and LM and the scalar character for the remaining variables are specified by proper selection of the parameter ITYPE in the subroutine. All the variables are being advected at the Eulerian remap step except for the last two, which are demanded by appropriate selection of the parameter IADVCT for the variables defined above (see [19]). The dimensioning parameter (array RDIM [19]) is set up in accordance with the physical nature of the extra variables. The initial data for all the variables except the mass and volume concentrations and the old density are set to zero. The initial data for these concentrations and the density are taken from the values determined in the UINCHK (more precisely, in the VERCHK) subroutine.

## 4.2 Lagrangian Block

For the second LB part of the code, two subroutines of the main LB subroutine ELSGE are involved in the modifications. The first is the database one processing subroutine, ELSGD, and the second is the main processing subroutine ELSG [5, 9, 10, 19].

#### 4.2.1 ELSG modifications

A database (DMB) subroutine dealing with the ELSG subroutine is modified to increase the number of scratch arrays that are necessary for processing all the extra variables by setting the relevant variable (the number of scratch arrays) to a larger value for the present model. The ELSG subroutine that is the main CE driving part of the CTH code processes the stress tensor equations taken in the Jaumann derivative form [20]. The equations for the deviatoric part of the stress tensor are an analogue of the equations (2) of the model. The initial stage of the ELSG modifications extracts both the symmetric and the skew-symmetric parts of the velocity gradient at an advanced half time step [20]  $t = t_{n+\frac{1}{2}}$ , density at the new time step  $t = t_{n+1}$  and pressure, temperature, and stress deviators at an old time step (at the start of the time cycle calculation)  $t = t_n$ . Extra variables, namely, mass, volume, and entropy disequilibrium concentrations, as well as ‘specific’ strain, the strain disbalance, and density and entropy at the old time step are retrieved and the extra variable update is conducted. As a result, the main driving subroutine VERDRV specified for local DMB-extracted arguments as VERSIG

## UNCLASSIFIED

DSTO-TR-2728

performs the following: i) within VERSIG, the extra variables for mass, volume and entropy disequilibrium concentrations are calculated by subroutine VEREXD, and ii) the stress deviator for the second constituent is calculated using equations deduced similarly to [5] in the manner that the system (21) is obtained where  $G_2$  should be taken at an advanced half time step. These calculations are followed by calculations of the 'specific' strain and strain disbalance using subroutine VERRXL for calculation of the stress return to the yield surface.

Summarizing, the model modifications of the ELSG subroutine include the calculation of: i) the modulus  $G_2$  at  $t = t_n$ ; ii) the invariant  $d$  of the tensor  $e_{ij}^{(2)}$  from (11) at  $t = t_n$ ; iii) the Gibbs potentials and the potentials  $\Lambda$  and  $\Pi_0$  from (8) at  $t = t_n$ ; iv) the mass, volume and entropy disequilibrium concentrations at  $t = t_{n+1}$  using the subroutine VEREXD; v) the shear stresses  $s_{ij}^{(2)}$  at  $t = t_n$ ; vi) the modulus  $G_2$  at  $t = t_{n+1/2}$  as an average of  $G_2$  at the old and new time steps; vii) an intermediate stress deviator  $s_{ij}^*$  using the elasticity equations (ignoring the relaxation terms in the stress equations); viii) the intermediate stress intensity according to  $(s^*)^2 = s_{ij}^* \cdot s_{ij}^*$  for the second phase; ix) the scaling factor of the stress deviator (the yield return) using the subroutine VERRXL; and x) the stress tensor  $s_{ij}^{(2)}$  at  $t = t_{n+1}$  followed by calculations of  $e_{ij}$  and  $\lambda_{ij}$ .

Briefly specifying VEREXD, the mass concentration does not change in the present implementation due to absence of mass exchange between the phases in the porous material; the volume concentration is calculated from (4) as  $d\theta/dt = -\psi$  within the Lagrangian step with  $\theta$  taken at the new time step inside  $\psi$  defined from (9), (23); and the entropy disequilibrium is calculated from (5) as  $d\chi/dt = -\omega$  within the Lagrangian step with  $\chi$  taken at the new time step inside  $\omega$  defined from (9), (18).

Calculations of the subroutine VERRXL are practically identical to the stress relaxation calculations realised for the decoupled Maxwell-type model and described in [5]. Namely, using the elastic trial stress  $s^*$  mentioned above as an initial data point within the Lagrangian step for the equation  $ds/dt = -s/\tau_2$ , we can calculate the stress intensity  $s$  at  $t = t_{n+1}$  (see [5] for details). The stress deviators are calculated afterwards in the standard fashion:

$$s^{n+1}_{ij} = (s^{n+1}/s^n) \cdot s^n_{ij}.$$

In the constitutive equation calculations outlined above, new values of the concentration parameters and the stress invariant at  $t = t_{n+1}$  are calculated by iterations, using Newton's method.

Thus, the whole set of the extra variables  $c$ ,  $\theta$ ,  $\chi$ ,  $e_{ij}$  and  $\lambda_{ij}$  is calculated in the present subroutine for the Lagrangian step. However, the variables have to be updated on the Eulerian remap step after advection and used afterwards for calculation of the remaining thermodynamic parameters using EOS at the end of the time cycle calculation.

### 4.3 Eulerian Remap Block

The modification in the ERB block deals with the EREB subroutine [5, 9, 10, 19]. Three parts of this modification deal with i) preparation of the extra variables for the thermodynamic

## UNCLASSIFIED

processing; ii) EOS modification to the present model's EOS; and iii) adjustment of the extra variables to the present thermodynamics state using the advected values [21].

#### 4.3.1 EREB modifications

The first part of the modifications calls subroutine VERSWP. The subroutine replaces values of the whole set of 13 thermodynamic extra variables defined in EOSVEK and accessed via the EOS substitute subroutines by values of the first 13 (out of the whole set of 15) variables defined in the UINSIV subroutine and accessed via the CE subroutines. These variables have been updated in the ELSG subroutine on the Lagrangian step (see the previous subsection).

The second part of the modifications is dealing with EOS used in the following two forms admissible by the CTH code: the energy form and the temperature form (see [22]). The corresponding substitute subroutines EOSVEV and EOSVES have been modified for the present EOS. In order to satisfy the variable choice requirement, the present EOS needs to be reformulated in the density-energy and density-temperature forms. This is done by using (6), (7), (10), (11) and (14). To facilitate the calculations, entropy is calculated in these subroutines from the internal energy or temperature by iterations using Newton's method. The subroutines must calculate the following derivatives of dependent thermodynamic variables, namely,  $(\partial p / \partial \rho)_T$ ,  $(\partial p / \partial T)_\rho$ ,  $(\partial e / \partial \rho)_T$ , and  $(\partial e / \partial T)_\rho$ . Here energy,  $e$ , is a function of  $\rho$  and  $T$ . The derivatives are obtained by the standard thermodynamics rules using the internal energy potential  $e(\rho, S)$  from derivatives over  $\rho$  and  $S$ . For example,

$$(\partial e / \partial \rho)_T = (\partial e / \partial \rho)_S - (\partial e / \partial S)_\rho (\partial T / \partial \rho)_S / (\partial T / \partial S)_\rho .$$

The remaining derivatives are obtained in a similar manner.

After the energy update at the thermodynamics-processing module of the Eulerian remap block in EREB, the last part of the modifications finalises preparation of the extra variables for the next time step. Specifically, using the internal energy, density and advected stress and the extra variables that are common to the EOS and EP groups, entropy is calculated from EOS and along with the density is stored as the two last variables of the EP group in order to have these variables in the ELSG subroutine at the start of processing the next time cycle.

## 5. Shock Propagation in Highly Porous Material

The first set of test calculations simulates plate impact experiments in the one-dimensional set-up. This modelling is aimed to check out if the present implementation is capable of describing the anomalous behaviour of highly porous materials. This behaviour is well known for the majority of porous substances at high and extreme porosities and manifests itself at the shock loading of porous samples as decreasing density behind the shock front when the pressure increases in a certain pressure range.

## 5.1 Parameters and Hugoniot of Silica

The specific purpose of the present implementation was the description of sand subject to loading by a detonating charge. Therefore, this specific porous material is under consideration in the present work. A further modification of the implementation for the description of the shock behaviour of a few metallic powders with the constitutive relations taken from [4, 6-7] is a routine procedure. Turning to sand, the solid constituent of this porous mixture is silica. The pressure-density dependences behind the shock front (Hugoniot) are reported for many porous substances including porous silica. Hugoniots for silica taken from paper [11] are shown in Fig. 1 at the initial material densities  $\rho_0$  of 0.4 and 1.55 g/cm<sup>3</sup>. It is seen from Fig. 1(a) that at the high porosity  $m$  more than 6 ( $m = \rho_0s/\rho_0$ ) if  $\rho_0 = 0.4$  g/cm<sup>3</sup> (for polycrystalline quartz as the solid constituent,  $m = \rho_0s/\rho_0 = 2.65/0.4 = 6.625$ ), the Hugoniot demonstrates anomalous behaviour in the pressure range between 5 and 20 GPa. Besides, the silica material appearing in nature as quartz is a material manifesting more complex behaviour than many metals. In particular, silica is subject to a few high-pressure phase transitions to polymorphs that have a significantly higher reference density than crystalline or amorphous quartz at the ambient pressure (see Fig. 1(b) for schematics of the static pressure-temperature phase diagram).

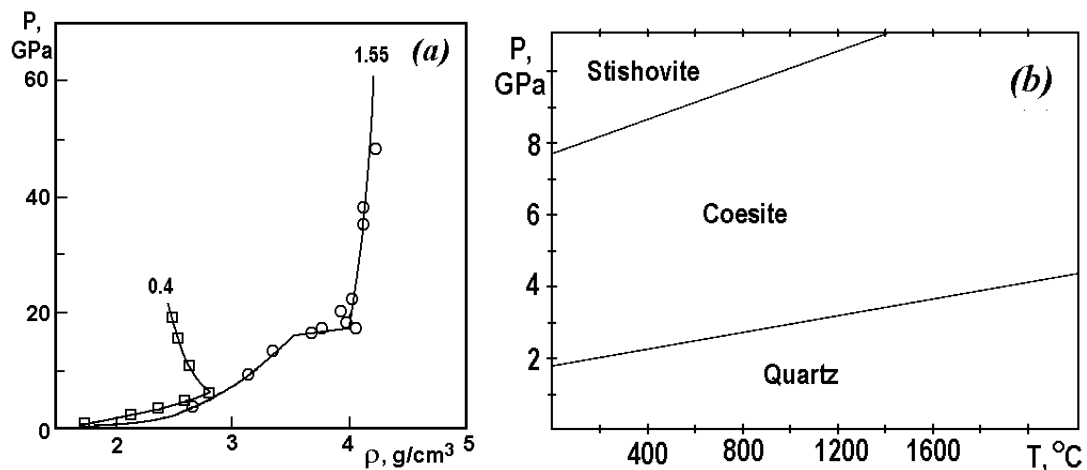


Figure 1. Experimental Hugoniots of porous silica at two initial densities [11] (a) and a simplified schematic of the silica phase diagram (b)

It should be noted that the simplified diagram in Fig. 1(b) ignores numerous high-temperature polymorphs for the sake of simplicity because reference densities of these polymorphs are quite close to that of the quartz at the ambient pressure and temperature (the  $\alpha$ -quartz for the polycrystalline material). Comparing the  $\alpha$ -quartz with its high pressure polymorphs, the first high pressure polymorph, coesite, shows at least a 10% reference density increase and the second one, stishovite, more than 60%. Taking into account a phase transition within the solid constituent would require a three-phase model such as [1] for a single transition and a multi-phase model with four or more phases for additional phase transitions. The present implementation takes a simplified approach with a single solid phase in order to remain within the two-phase model framework.

The ability of the present model to describe behaviour of highly porous metals has been demonstrated in papers [4, 7], using an in-house code based on the Godunov method. One-

dimensional calculations with this code were verified against plane impact data on the shock behaviour of a few porous substances. Because of the simplified description of sand in the present work, the following flowchart will be used for verification of the present implementation. For the critical case of a highly porous silica, a one-dimensional calculation will be conducted using the code [4, 7]. After that, results of the calculations will be compared with the modelling results obtained with CTH using the present implementation.

First of all, the material constants for the two-phase model have to be specified in a form that is practically identical for both the code [4, 7] and the present CTH implementation. The parameters to be used are listed in Subsection 4.1.3. Amongst them, a number of constants are well determined such as the sound velocity and polytropic exponent of the air:  $c_0 = 0.34$  km/s and  $\gamma = 1.4$ , and the ambient pressure,  $p_0 = 1$  bar. For quartz, the heat capacity is taken from [23]  $c_{vs} = 0.75$  J/g/°K with the solid density  $\rho_{0s} = 2.65$  g/cm<sup>3</sup> for polycrystalline quartz and  $\rho_{0s} = 2.2$  g/cm<sup>3</sup> for fused quartz. The initial density of porous silica to be used in the one-dimensional calculations is  $\rho_0 = 0.4$  g/cm<sup>3</sup>. The shear modulus  $G = 31.2$  GPa and the bulk modulus  $K = 37.2$  GPa. The modulus' pressure derivatives from [24] along with the Hugoniot data [25] give:  $a_0 = 4.057$  km/s;  $b_0 = 3.43$  km/s;  $a_0 = 0.1$ ; and  $\beta_0 = 1$ . While varying somewhat with density in reality, the Grüneisen coefficient is taken as a constant  $\gamma_0 = 0.55$  from [26] for the pressure range of interest. The strength data for quartz vary in the literature within a quite wide range from tens of MPa to a few GPa. Therefore, as a plausible choice in the static-dynamic range for a quite wide span of strain rates:  $\dot{\varepsilon}_1 = 10^{-2}$ s<sup>-1</sup>;  $\dot{\varepsilon}_2 = 10^3$ s<sup>-1</sup>, we take the yield limit values as  $Y_1 = 200$  MPa;  $Y_2 = 400$  MPa at compression. At tension, the Y-values would be more reasonable, in fact, to relate to a sandstone rather than to a polycrystalline or fused quartz material, thereby reducing these values by an order or so (e.g. see [27, 28]). For the shock loading tests used for verification of the behaviour of the highly porous sand, we are mostly interested in the compression state of the material. Therefore, we arbitrarily take  $Y_{1t} = Y_1$ ;  $Y_{2t} = Y_2$  in the one-dimensional calculations. The solid defects constants in (15) are taken as  $N_0 = 10^4$  and  $M = 10^6$ . The compaction kinetics constants in (23) are chosen to be identical to those from [6]:  $\theta_{00} = 0.25$ ;  $p_c = 1.25$  GPa;  $n_c = 4$ ;  $\psi_{00} = 15$  s/m<sup>2</sup>. For the heat transfer kinetics we take the grain size as  $d_0 = 0.1$  mm and the heat conductivity constants for the air and quartz as  $k_1 = 0.025$  W/m/°K and  $k_2 = 2$  W/m/°K with the dimensionless coefficient  $A_S = 400$  ( $d_0$  and  $A_S$  are interrelated when mutually changing; see [4] for details).

## 5.2 Shock compression calculations using verified code

For one-dimensional calculations of the highly porous silica we choose the constants above with the initial solid density corresponding to the polycrystalline quartz. Ignoring the phase transitions in quartz, we can evaluate 'partial' Hugoniots of the porous material using the technique [7] while keeping various thermodynamic parameters at equilibrium.

## UNCLASSIFIED

DSTO-TR-2728

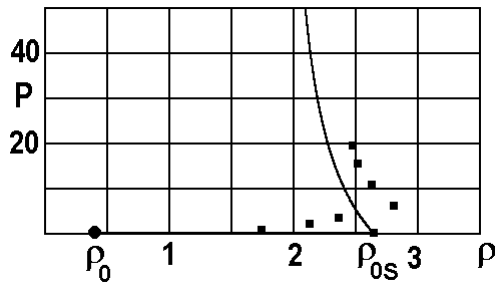


Figure 2. Calculated PTE Hugoniot (solid curve) at the pressure-temperature equilibrium [7] compared with the experimental Hugoniot data (points [11])

Traditionally, the Hugoniot of a multi-phase material is a locus of states behind the shock front that are considered to be in thermodynamic equilibrium between the material phases. However, as noted in [7], this is not always the case. At certain levels of loads some thermodynamic parameters between the phases may be in equilibrium, whereas the others are not. Thus, a variety of Hugoniots can be derived and depending on the meso-mechanics of a multi-phase material one Hugoniot from the variety can supersede another, resulting in a composite Hugoniot for a real material under shock loading (see [1, 4, 6, 7] for details and examples). Specifically, for some typical thermodynamic parameters Hugoniots are referred to as PE (Pressure Equilibrium) and PTE (Pressure-Temperature Equilibrium) Hugoniots (other Hugoniots are also possible, see [1, 4, 7] for details). For the present case, where the nature of equilibrium is changing during shock loading, the anomalous pressure-density behaviour behind the shock front (the PTE Hugoniots are usually anomalous for highly porous mixtures) supersedes the conventional behaviour (the compaction stage). For illustration, the calculated analytical PTE Hugoniot of sand at  $\rho_0 = 0.4 \text{ g/cm}^3$  shown in Fig. 2 by a solid curve manifests the anomalous behaviour. However, as mentioned above, this behaviour is only a part of the whole picture. Different porous mixtures realize different mechanisms of transition from one regime to another.

The highly porous silica demonstrates a relatively low point of transition to the anomalous path. This is likely to happen immediately after compaction. Thus, the experimental points in Fig. 2 demonstrate the anomalous behaviour above 5 GPa and conventional behaviour below this point, where the compaction curve reflects the conventional relationship of density rise with pressure increase. It should be kept in mind, that the density shift of the calculated Hugoniot from the experimental points in Fig. 2 is possibly associated with a phase transition, and it is not taken into account for the sake of simplicity. However, an attempt to simulate the switch from the conventional to the anomalous behaviour observed in the experiments shown in Fig. 2 will be undertaken.

UNCLASSIFIED

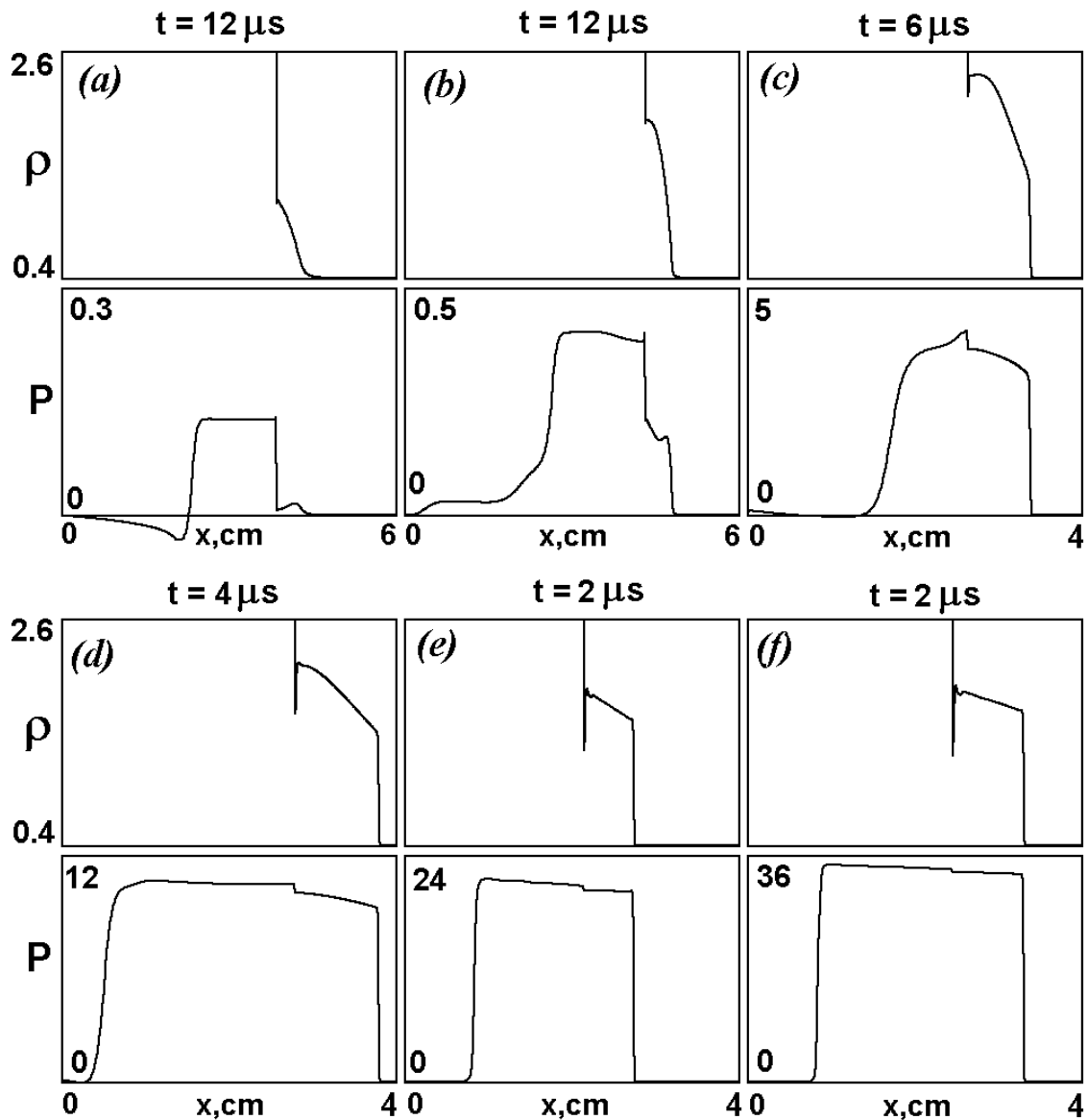


Figure 3. Numerical results for the porous sand using the code [4]

The first calculation is conducted with the one-dimensional in-house code [4, 7] based on the Godunov method [29]. This code has been verified for a few porous and condensed two-phase mixtures [4, 6, 7] using relations including, but not limited to the constitutive functions described above. Numerical results obtained with this code are shown in Fig. 3 for the high velocity impact set-up with a copper flyer plate and a target representing a layer of sand. Thicknesses of the flyer plate ( $h_f$ ) and the sand sample ( $h_s$ ) are  $h_f = 2.5$  cm,  $h_s = 3.5$  cm (a-b) and  $h_f = 1.5$  cm,  $h_s = 2.5$  cm (c-f). The velocities of impact,  $U_0$ , in km/s for Figs. 3(a-f) are 0.5 (a); 1 (b); 3 (c); 5 (d); 7 (e), and 9 (f). The calculation is conducted in adaptive grids with the combined computational domain (flyer plate plus target) rescaled back for the sake of visualisation to the initial domain as shown in Fig. 3. The free and contact interfaces in these calculations are Lagrangian and internal nodes – Eulerian (see [29] for details). For simulation of the flyer plate, the viscoelastic model [17] has been used with the material constants for copper taken

from [13]. Snapshots of the density and pressure profiles are shown at the same time points for each of the impact velocities (the time marks are shown above each of the graphs). Tracing the pressure and density states behind the shock front in sand, it is seen that when pressure is rising, density is first increasing in the pressure range below 5 GPa (plots in Fig., 3(a-c)) and then decreasing at further increase of pressure (plots in Fig., 3(d-f)). This behaviour agrees quite well with the experimental behaviour shown in Fig. 2, following the trend of the initial conventional compaction path superseded by the anomalous PTE Hugoniot.

### 5.3 Shock compression calculations using the CTH implementation

Calculations with CTH using the present implementation require specification of the sand material in the both sections of the input deck associated with the EP and EOS blocks. The corresponding specification in the 'eos' section refers to VE EOS subroutines that are substituted in the present implementation by the subroutines described in the previous section of the report.

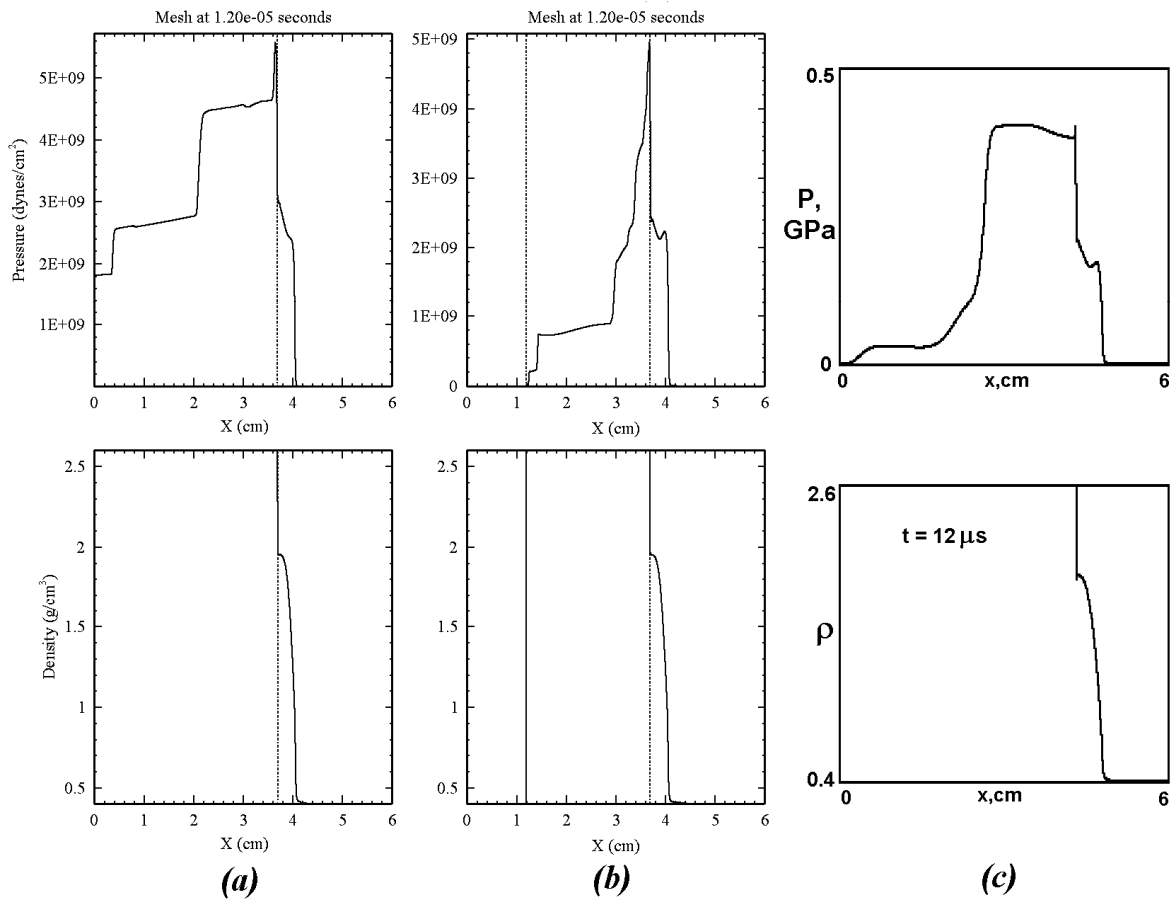


Figure 4. Comparison of the CTH calculations in the underlying (a) and control (b) set-ups with the profiles calculated using the code [4, 7] (c)

This reference forces CTH to retrieve information about any material from the EOS\_data material database associated with the VE model (for example, in a fragment of the input deck

below, the 'pmma' material is referred to). Because of the substitution this information cannot actually be utilized when the implementation is active with the exception of the first three constants. In fact, only these three constants are important for the corresponding implementation subroutines in order to start proper processing of the EOS input and initialisation blocks. After processing of the EP input block, the whole set of constants is determined and correctly placed for subsequent calls of the EOS modules. These three constants taking the roles of the mixture density, and densities of the gaseous and solid phases are 'R0', 'T0', and 'CV', respectively, referring to the VE input nomenclature. The processing of the EP input data is conducted in quite a conventional way in CTH through reference to the present model name, 'VER'. Specification of one of the constants, namely, the material density (unless this density is coincident with the one from the dataset called by the material name specification), is mandatory, whereas the whole set of the EP input constants is summarised in the VP\_data file. This data set is taken from the rows of the VP\_data file identified by the material name and it contains 37 constants described in Subsection 4.1.3.

For example, assuming that the material's '2' name is 'SAND', and its initial density  $\rho_0 = 0.4$  g/cm<sup>3</sup>, the required fragment of material specification in the input deck for the material described by the present two-phase model should appear as follows

```

eos
  mat2 ve pmma R0=0.4 T0=0.00121107266 CV=2.65
endeos

epdata
  matep 2 VER SAND RHO = 0.4
endepdata

```

To remind, the initial density of the air  $\rho_{0g} = 0.00121107266$  g/cm<sup>3</sup> is actually calculated on the processing stage of the EP input block and specified here only for the correct initial processing of the EOS input and initialisation blocks. Therefore, this density is calculated beforehand and used as the datum 'T0' above. For the same purpose, the initial density of the solid phase  $\rho_{0s} = 2.65$  g/cm<sup>3</sup> is also taken from the datum 'CV' above. It should be noted that this twist is unnecessary if proper access to the EOS block is available. In that case, new EOS name can be specified and used for the present model. Therefore, the model could be realised with its own specifications instead of using the name, VE, of the subroutines substituted and the names of VE variables for substitution in the data set, when the relevant 'eos' section in the input deck is activated.

The high-velocity plane impact set-up for CTH employs similar input conditions as in the previous calculation. The computational one-dimensional Eulerian domain is separated into two zones: i) a flyer plate with the thickness  $h_f$  of either 2.5 or 3.5 cm depending on the impact velocity, similarly to the previous subsection set-ups; and ii) the sand sample zone (a target) with the thickness  $h_s$  of either 1.5 or 2.5 cm, respectively. Due to the purely Eulerian nature of the code, the boundary conditions require more attention than in the previous case. In the CTH simulations below, the left boundary condition was usually taken as the inflow condition that enabled the rarefaction wave from the rear side of the flyer plate to come to the projectile-target interface later than in the case of the free surface condition. However, this choice did not affect the density value behind the shock front. This point has been checked out by special control calculations with the free surface conditions.

## UNCLASSIFIED

DSTO-TR-2728

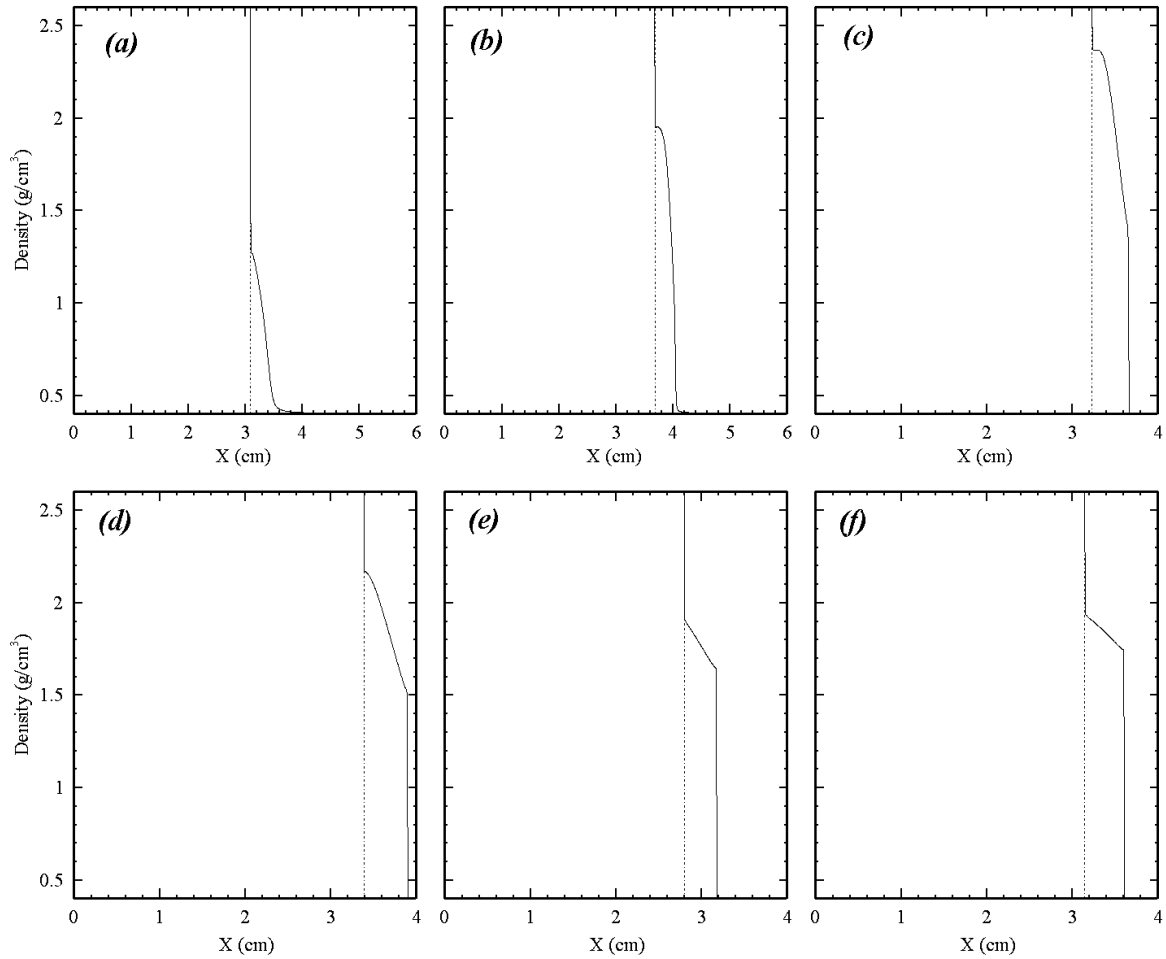


Figure 5. CTH calculations of the density profiles in the porous sand at various impact velocities

In the CTH calculations, a model for the description of the copper material of a flyer plate is the Steinberg-Guinan-Lund model [3]. Results of comparison of the CTH calculations using the present implementation at  $U_0 = 1$  km/s with the set-up described above (a), with a control set-up with the free surface boundary conditions (b), and the calculation from the previous subsection (c) are shown in Fig. 4. It is seen that all these calculations result in nearly identical density profiles in the sand sample. The pressure profiles for the same boundary conditions (Figs. 4(b) and (c)) are close. It should be kept in mind the visualisation convention in Fig. 4(c), where the external free boundaries are rescaled back to the initial positions with the contact interface having changed its position between the external free boundaries by  $t = 12$   $\mu$ sec, whereas the CTH visualisation in Figs. 4(a-b) refers to the actual boundary positions within the fixed grid. The observed pressure jump at the projectile-target interface is associated with the strength effects because the stress equilibrium at the interface is satisfied only for the longitudinal component of stress.

The density profiles from the CTH calculations using the present model implementation at the same impact velocities as in the previous subsection ( $U_0$  in km/s are 0.5(a); 1(b); 3(c); 5(d); 7(e); and 9(f)) are summarized in Fig. 5 for the boundary conditions of the underlying set-up (as

UNCLASSIFIED

that of Fig. 4(a)). When comparing the corresponding profiles from Figs. 3 and 5, it is seen that the profile features in sand such as the peak density and the character of ramping are practically identical for these two series of calculations. Thus, this comparison gives us a confidence in the adequacy of the present numerical realisation within the CTH implementation framework.

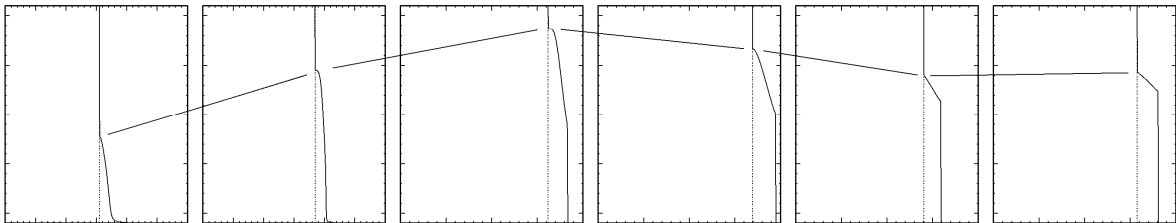


Figure 6. Summary of the Hugoniot densities calculated with CTH using the present model implementation

The numerical data summarised from Fig. 5 are drawn in Fig. 6 as a single graph with the straight lines characterising the trend of the behind-shock density change with the pressure rise from left to right. This trend shows the physical adequacy of the implementation (within the accuracy of chosen EOS), when comparing the calculated behind-shock (Hugoniot) densities, following a composite Hugoniot from the compaction pressure-density curve superseded by the anomalous PTE Hugoniot, which correlates quite well with the Hugoniot response observed experimentally [11] (see Fig. 2).

#### 5.4 Shock compression calculations using models available in CTH

The CTH calculations using the present model can also be compared with CTH calculations employing porous material models available in the CTH model database [3]. The CTH models that may associate most closely the thermodynamic states of a material with EOS experimental data are those of the SESAME family [30]. The SESAME EOS database describes the material state response in a tabulated form with necessary interpolations between the state database nodes. However, a disadvantage of this approach is that any out-of-node state is a calculated extrapolation of the tabulated data and, if not in close proximity to the table data, this approximation relies on extrapolation algorithms rather than on physics laws. A relevant model from the SESAME database is the DRY SAND model (in fact, a table extrapolation) complemented with the P-alpha EOS reduction rule [3] used for the porous material description. Because this description extrapolates a behaviour between the EOS data nodes tabulated by experiment, it is expected that the pressure density abnormalities are somewhat covered by the DRY SAND model prediction. The second model is the P- $\lambda$  model by Grady that describes the non-linear response using a composite EOS in a kinetic manner managed by the compaction parameter  $\lambda$  [31].

## UNCLASSIFIED

DSTO-TR-2728

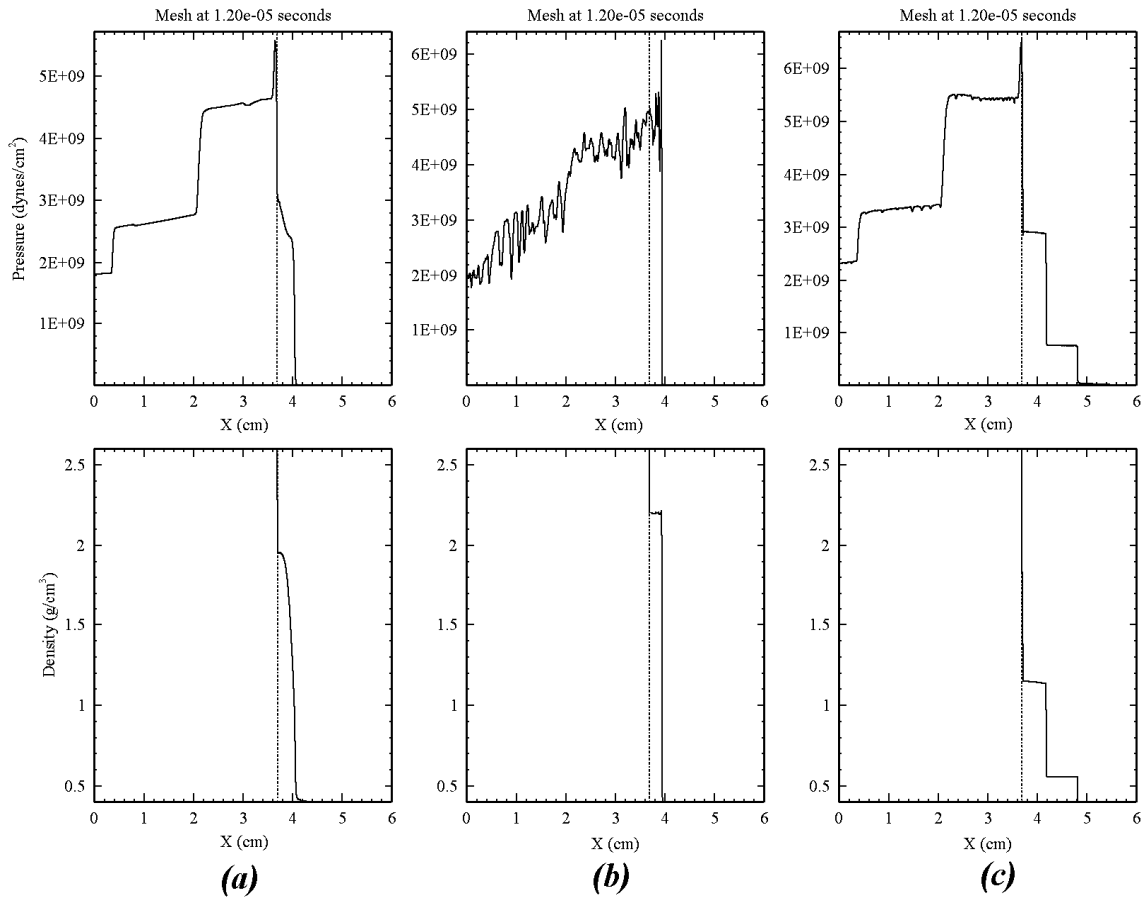


Figure 7. Comparison of the numerical results for the present model (a) with those for the DRY SAND (b) and P- $\lambda$  (c) models of CTH

The pressure and density profiles taken from the previous subsection and calculated using the present two-phase model at the impact velocity of  $U_0 = 1$  km/s are shown in Fig. 7(a). These calculations are compared with the profiles within the same set-up, which are calculated using the DRY SAND model (Fig. 7(b)) and P- $\lambda$  model (Fig. 7(c)). It is seen that the tabular EOS response based on the SESAME approach in Fig. 7(b) manifests an oscillating pressure profile behind the shock front fed into the pressure pulse propagating back to the flyer plate. In turn, the response obtained with the physics-based P- $\lambda$  model in Fig. 7(c) results in a quite similar pressure profile in the flyer plate when compared with that of the present two-phase model in Fig. 7(a). The pressure amplitude, however, is obtained from the model-specific EOSs, therefore, it is not expected to be identical for these models. At the same time, the density profiles in sand are quite different for all the three models.

UNCLASSIFIED

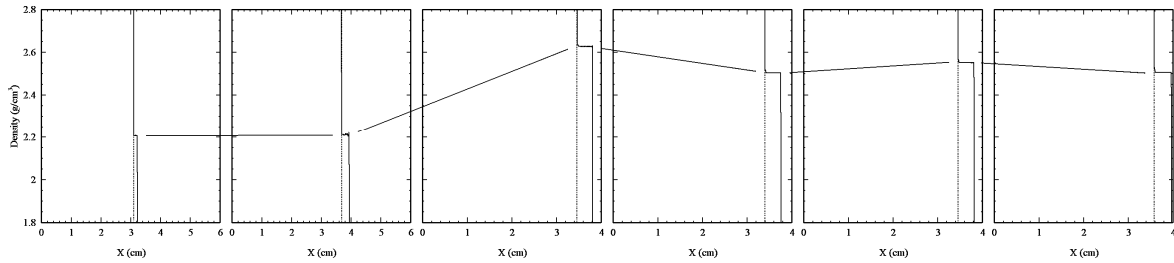


Figure 8. Trend of the Hugoniot densities versus pressure calculated with the DRY SAND model

The density profiles calculated with CTH using the DRY SAND model at the same impact velocities as in the previous subsections are summarised in Fig. 8 in the same manner as in Fig. 6. It can be seen that the tabular character of the SESAME EOS, resulting in a somewhat oscillating response, transmits this response to the density trend at high pressure. However, in the middle of the pressure range the correct abnormality trend still remains, namely, the maximum density is reached at the impact velocity of  $U_0 = 3$  km/s (the third graph from the left in Fig. 8), corresponding to the peak pressure of approximately 5 GPa (see Hugoniot data in Fig. 2).

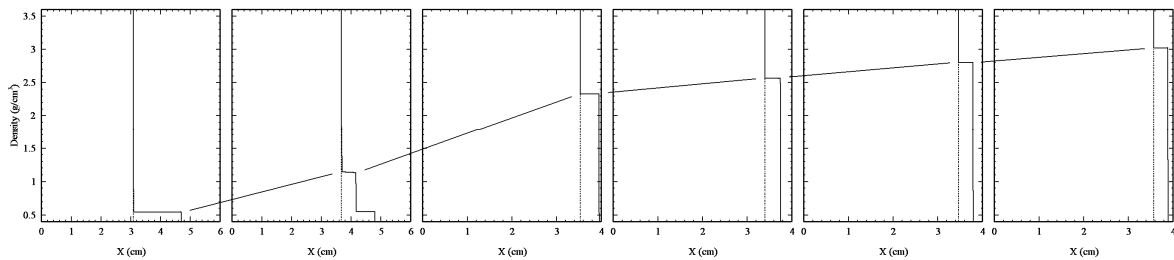


Figure 9. Trend of the Hugoniot densities versus pressure calculated with the P- $\lambda$  model

The next model prediction with a regular EOS such as that of the P- $\lambda$  model does not demonstrate any abnormality. The corresponding CTH results are shown in Fig. 9 and the density trend is quite conventional with the density and pressure increasing concordantly. Obviously, this trend does not correlate with the experimental data shown in Fig. 2.

## 6. Buried Charge Modelling

In the mine blast experiments, total momentum is often recorded by using a momentum-measuring device (e.g. pendulum). However, the major contribution to the total momentum is due to loading by the detonation products, while the major contribution to the stress pulse transferred to the target is due to the ejecta impact. Therefore, in order to take into account the highly dangerous, although short-time ejecta contribution, the soil ejecta formation and momentum transfer by the ejecta to a target should be considered. As mentioned in the Introduction, the velocity-density distribution through the ejecta thickness is the decisive information for evaluation of this contribution. This information, however, is not readily available. The peak stress in the stress pulse travelling through the target is associated with the impact velocity of the soil ejecta. The length of the pulse and the pulse fluctuations could

## UNCLASSIFIED

DSTO-TR-2728

be obtained from the velocity-density information. Nevertheless, as a first step in the evaluation, the velocity can accurately be estimated from high-speed video or pulse x-ray shots. CTH calculations in the present section are aimed at analysis of the experimental observations made with the pulse x-ray experiments [12] on the explosion of 100g C4 charges buried under a layer of sand.

## 6.1 The problem statement

The experimental results [12] are simulated within the axi-symmetrical two-dimensional set-up. The experiments [12] deal with a cylindrical volume of sand of approximately 88 cm in diameter and 70 cm in height that is not confined at the upper side of the volume (i.e. it is in the contact with air) and is contained laterally and at the bottom by a steel case. The present numerical set-up considers one half of the whole experimental set-up in the radial direction away from the symmetry axis with rigid boundary conditions sidewise and at the bottom. 20 cm of air space is within the chosen computational domain. The observation area subject to graphical output is 40 x 40 cm with the centre at the intersection of the symmetry axis and the air-sand free surface interface. This observation area is marked by the square in the set-up graph of Fig. 10 for the whole set-up geometry (the actual observation area in the calculation set-up is 20 x 40 cm), which approximately corresponds to the experimental observation area [12].

Two Depths Of Burial (DOB) for the High Explosive (HE) charges are considered in agreement with the buried charge set-ups of [12]: DOB = 3 cm and DOB = 8 cm. The C4 charge was simulated using the HE burn model [3] under JWL EOS for Composition C-4 (see [3] for details) with the JWL database choice of constants. The charge was selected to be cylindrical with a diameter of 6.4 cm and a height of 2 cm [12]. Two charge initiation configurations have been considered in [12] with detonation either (i) at the top or (ii) at the bottom of the charge. As found in [12], the first option generates a venting effect at the soil interface rendering this set-up inconclusive, whereas the latter is free of such limitations. Therefore, only the charge initiation configuration (ii) was considered in the present numerical set-ups. To approximate the experimental set-up the charge was encased in a 1 mm thick Nylon case described with a standard elasto-plastic model (von Mises criterion is used for the plastic flow simulation) with the yield limit of 500 MPa and the 'NYLON' SESAME EOS [3]. Similarly to the experimental set-ups, the charge was boosted by a 5 x 10 mm HE cylinder detonated from its lowest point at the axis of symmetry in the numerical set-up.

Material constants for the sand material modelled by the present CTH implementation are the same as those from the preceding subsection with the only adjustment to the fused quartz density value of  $\rho_{0s} = 2.2 \text{ g/cm}^3$ . This type of solid phase for calculations in this section is chosen because the EOS in the present case should cover a wider range of pressures, including those occurring at the rarefaction. Therefore, the Hugoniot shift to the higher density area seen in Fig. 2 might not be as critical for this porous material with a relatively low porosity opposed to the high porosity sand analysed at compression in the previous section. The choice of yield limits  $Y_1$  and  $Y_2$  is somewhat artificial because the yield limits are related only to the solid constituent and are not generally associated with the porous mixture. This choice was quite obvious in the preceding section because only the shock compression behaviour was considered and the yield limits were associated with the deformation (crush) of solid grains.

UNCLASSIFIED

The material densification can potentially be described by the compaction kinetic fitted at different modes of loading. Namely, in the case of cyclic loading and unloading of the porous material, the compaction kinetic,  $\psi$ , should be fitted by an analysis of solutions of (21) for specifically designed loading-unloading tests. Thus, this kinetic plays a key role in the analysis of this sort of problem. In the present work, we are forced to use the compaction kinetic fitted only to the compression mode of loading.

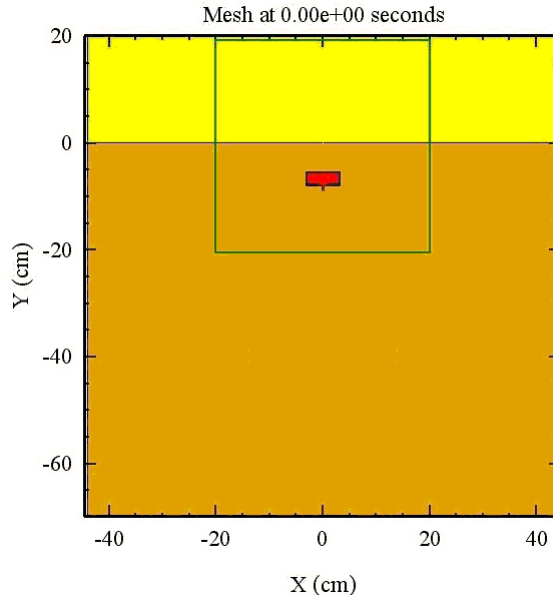


Figure 10. Schematic of the Buried Charge set-up

Therefore, we are trying to compensate the gap in determination of the compaction kinetic for this material, which significantly contributes to the behaviour of the soil ejecta, by a variation of the yield limits. In doing so, we assume that the behaviour of the porous material at unloading can be compensated by the deformation of the solid constituent, which is a very rough assumption. Several CTH runs have been conducted with various yield limit values at compression and tension, which are listed in Table 1. For completeness, even though they are unrealistic, the set-ups with a high strength at tension are included in the Table as well.

The initial average density of sand for all the cases calculated in this section is  $\rho_0 = 1.57 \text{ g/cm}^3$ , that corresponds to an average initial soil density in the tests [12]. The same porous material models from the CTH material model database as in the previous section have been selected for comparative calculations and listed in Table 1. As a reminder, the models are: the DRY SAND model from the SESAME EOS family with P-alpha model for the porosity simulation and the P- $\lambda$  model by D. Grady [31].

## UNCLASSIFIED

DSTO-TR-2728

Table 1. Modelling set-ups and yield limit values for the implemented model

N	Compression		Tension ( $p < 0$ )	
	$Y_1$ , MPa ( $\dot{\varepsilon}_1 = 10^{-2}\text{s}^{-1}$ )	$Y_2$ , MPa ( $\dot{\varepsilon}_2 = 10^3\text{s}^{-1}$ )	$Y_{1t}$ , MPa ( $\dot{\varepsilon}_1 = 10^{-2}\text{s}^{-1}$ )	$Y_{2t}$ , MPa ( $\dot{\varepsilon}_2 = 10^3\text{s}^{-1}$ )
DOB = 8 cm				
Run1	37.5	150	37.5	150
Run2	10	40	10	40
Run3	37.5	150	10	40
Run4	DRY SAND model [3]			
Run5	P-Lambda model [3]			
DOB = 3 cm				
Run6	37.5	150	37.5	150
Run7	10	40	10	40
Run8	37.5	150	10	40
Run9	DRY SAND model [3]			
Run10	P-Lambda model [3]			

Von Mises criterion of the traditional elasto-plastic model has been used for the DRY SAND runs with the yield limit of 10 MPa and for the P- $\lambda$  model with the yield limit of 500 MPa. These yield limit values provide the best fit between calculation results and the present experimental data within a reasonable yield limit range for quartz.

Table 2. Summary of the experimental data [12]

N	Time ( $\mu\text{s}$ )	DOB (cm)	Base width (cm)	1/3 width (cm)	2/3 width (cm)	Bubble height (cm)
12-1	230.9	8	19.9	13.0	9.4	2.9
12-2	301.1	8	22.9	14.5	9.8	4.3
13-1	351.0	8	27.9	16.1	11.1	5.2
13-2	401.1	8	29.1	16.7	11.9	6.2
14-1	451.0	8	32.8	17.7	11.8	6.9
14-2	526.1	8	31.1	17.6	12.4	8.2
16-1	100.8	3	17.3	11.5	7.8	6.5
15-1	100.9	3	17.7	12.3	9.8	8.4
17-1	125.9	3	19.9	13.1	10.1	8.8
16-2	201.1	3	22.0	17.3	13.8	16.4
17-2	201.1	3	24.6	17.3	14.3	16.5
15-2	201.9	3	24.2	20.7	18.5	19.2

The experimental results [12] are summarised in Table 2 showing the basic shape characteristics of sand ejecta for the two series of tests with  $\text{DOB} = 8\text{ cm}$  (3 tests with 2 snapshots for each test) and  $\text{DOB} = 3\text{ cm}$  (also 3 tests with 2 snapshots per test). The geometrical parameters taken from the x-ray shots are somewhat subjective but the Table is useful to see the test consistency and to evaluate the general appearance and velocity of the soil ejecta.

## UNCLASSIFIED

## 6.2 Calculations for Large Depth of Burial

The first series of calculations (runs from 1 till 5 in Table 1 that are further referred to as Run1-Run5) deals with identical mesh set-ups for the whole group of the five with DOB = 8 cm. This depth of burial is characteristic for conditions of the camouflet blast where the blast products are contained underground during the ejecta formation.

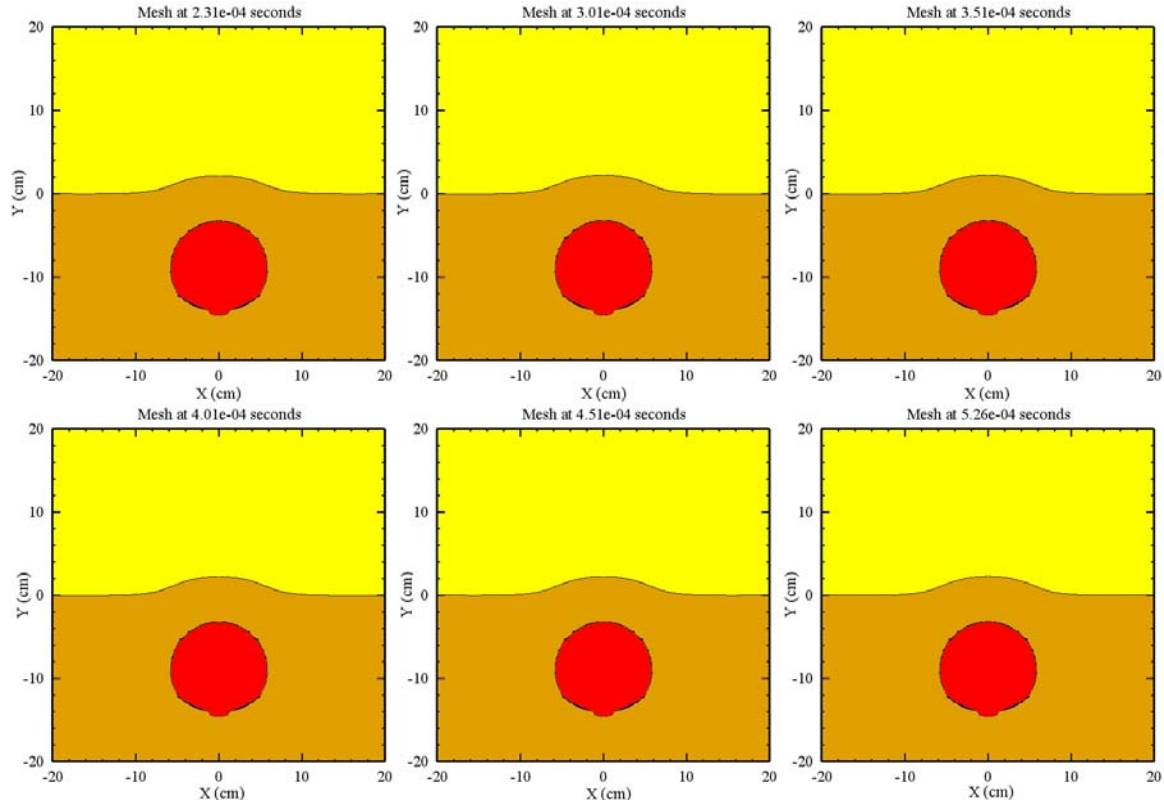


Figure 11. CTH calculation of the sand ejecta using the present model with parameters for Run1

Numerical results of the first calculation from this series (see Table 1), Run1, are shown in Fig. 11 at times approximately corresponding to those from the experimental observations shown in Table 2. It is seen that the material strength of the solid constituent equally high at tension and compression, which is approximately correspondent to that of non-porous quartz, has a significant and unrealistic constraining effect on the soil expansion. It is clear that the strength properties at tension should, at least, somehow differ from those at compression.

As mentioned in the earlier comments on Table 1, the compaction kinetic fit should, in fact, be responsible for the difference in the material compressibility of the grained porous sand at compression and at tension. Because the compaction kinetic selected for the compression case was not adjusted to the tension conditions in this work, the next step in the material properties adjustment was reduction of the material strength for the solid constituent.

## UNCLASSIFIED

DSTO-TR-2728

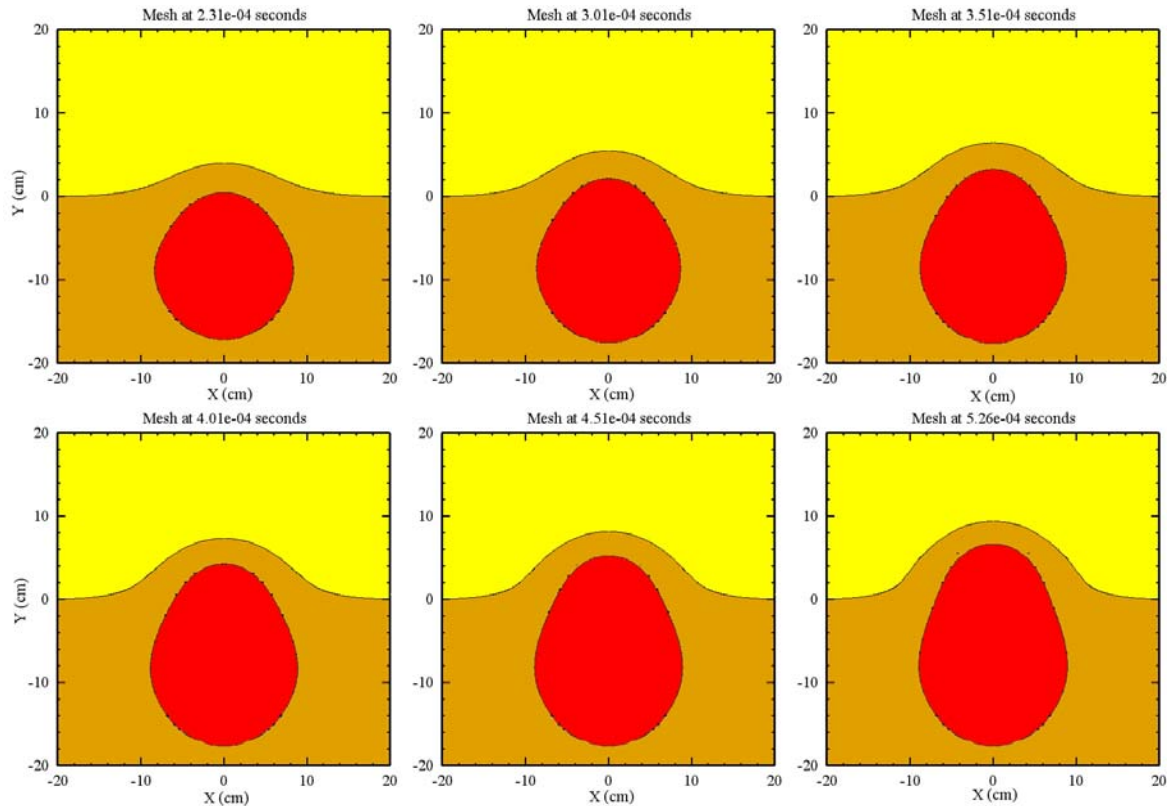


Figure 12. CTH calculation of the sand ejecta using the present model with parameters for Run2

For analysis of the influence of the strength reduction, the next calculation from Table 1, Run2, is conducted with the conditions of low yield limit at both compression and tension. From the results of this run, we can observe an extension of the soil ejecta both at the ejecta base and upwards resulting in a significant increase of the bubble height when compared with the previous set-up. Results of this modelling using the present implementation are summarised in Fig. 12, similarly to Run1 in Fig. 11.

For completeness of choice of the yield limit variations, the last option calculated within this series is calculation Run3 (Table 1) with high yield limits for the solid constituent at compression corresponding to the set-up of Run1 and the low yield limits at tension corresponding to the set-up of Run2. Numerical results for this run are summarised in Fig. 13 similarly to the previous cases.

## UNCLASSIFIED

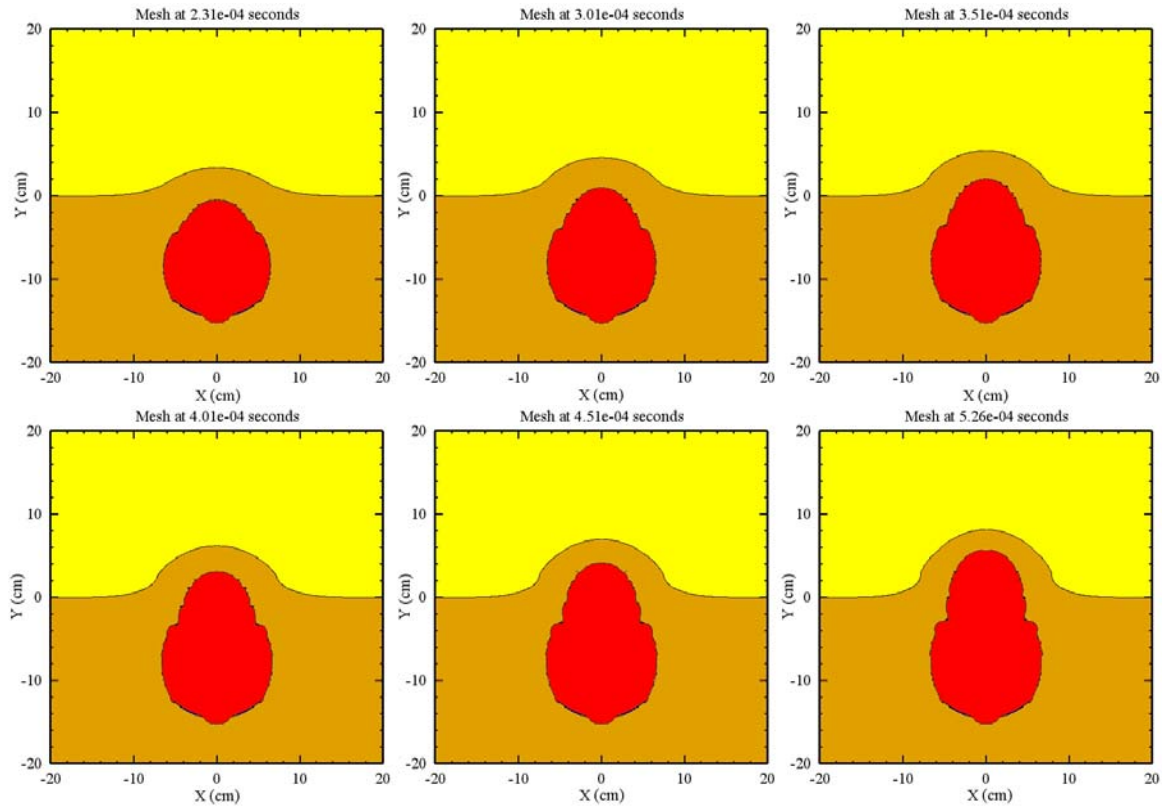


Figure 13. CTH calculation of the sand ejecta using the present model with parameters for Run3

Wrap up calculations of this series, Run4 and Run5, have been conducted with CTH using the material database models employing the DRY SAND model based on the SESAME EOS and the P- $\lambda$  model. Corresponding numerical results are summarised in Figs. 14 and 15, respectively. The P- $\lambda$  model results describe shapes of the ejecta bubble quite poorly and, therefore, only 3 snapshots are shown in Fig. 15 for comparison with the numerical results obtained with the other models.

Analysing the CTH results obtained with the present implementation (Figs. 11-13), we can see that the case of Run1 with very high constraining effects in Fig. 11 and the case of Run2 with significant relieving effects in Fig. 12 are separated by the case for Run3. When comparing the Run3 case (Fig. 13) with that of Run1 (Fig. 11), it is seen that the high yield limits at tension (with the same yield limits at compression) significantly affect the bubble height. At the same time, when comparing the Run3 case (Fig. 13) with Run2 (Fig. 12), it is seen that with the increase of the yield limit to the high values at compression (with the same yield limits at tension), the bubble height is almost unaffected and the base size is slightly restrained.

## UNCLASSIFIED

DSTO-TR-2728

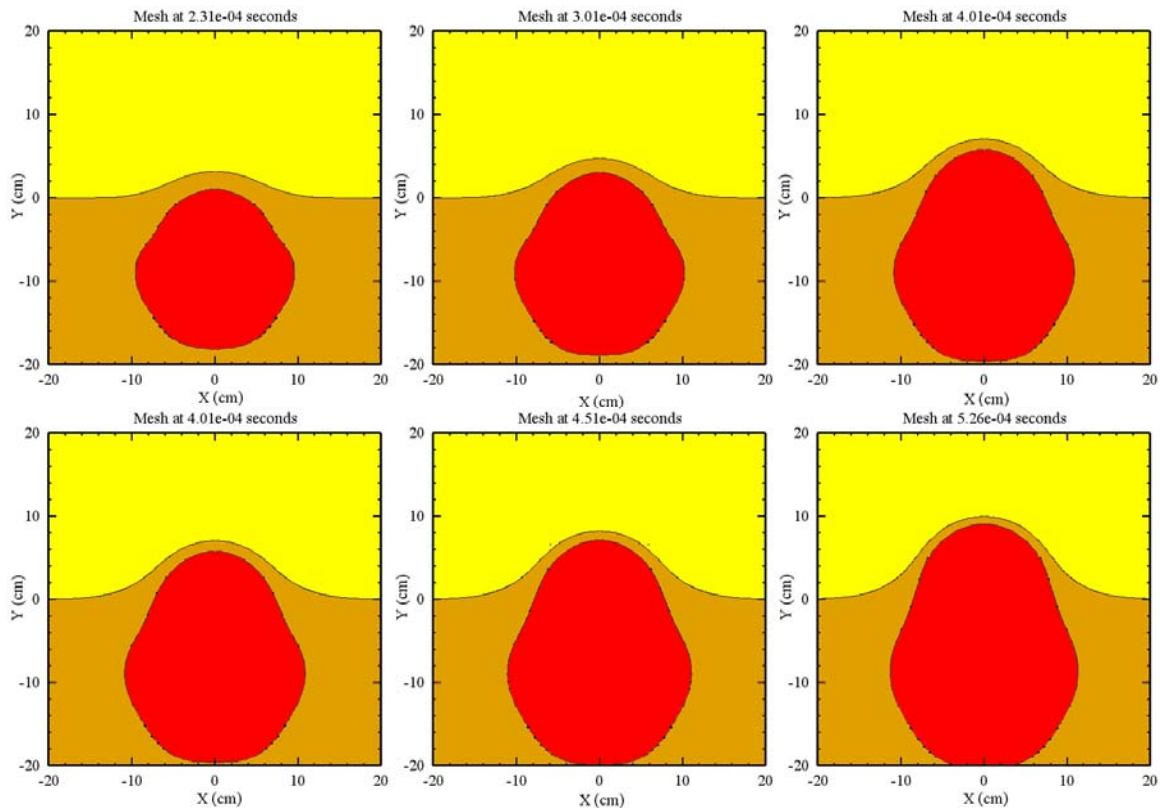


Figure 14. CTH calculation of the sand ejecta using the DRY SAND model (Run4)

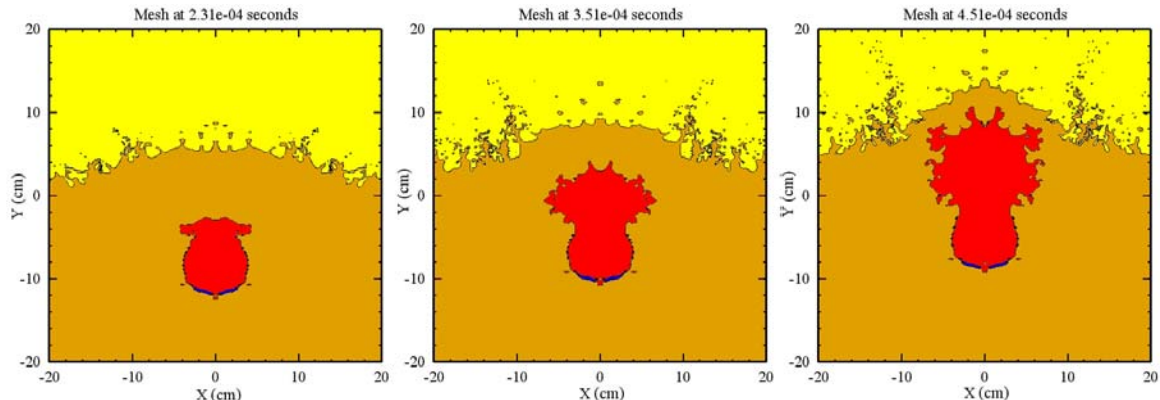


Figure 15. CTH calculation of the sand ejecta using the P-λ model (Run5)

In order to compare the results of the present series with the experiments, we superimpose the calculated external ejecta contours from Figs. 11-15 with the experimental snapshots [12] at the late stages of the ejecta formation. The results for the whole set of runs, Run1-Run5 (Table 1), are summarised in Fig. 16 (corresponding contours of the CTH calculations are referred to by the run names in each frame of Fig. 16). From the comparison, it is seen that the numerical results for Run2, Run3, and Run4 are in reasonable agreement with the experiment. The constraining effect seen in the Run1 graphs seems to be unrealistic, and choice between Run2 and Run3 can be done only after the appropriate fitting of the compaction kinetic which would also describe the unloading behaviour of the material.

## UNCLASSIFIED

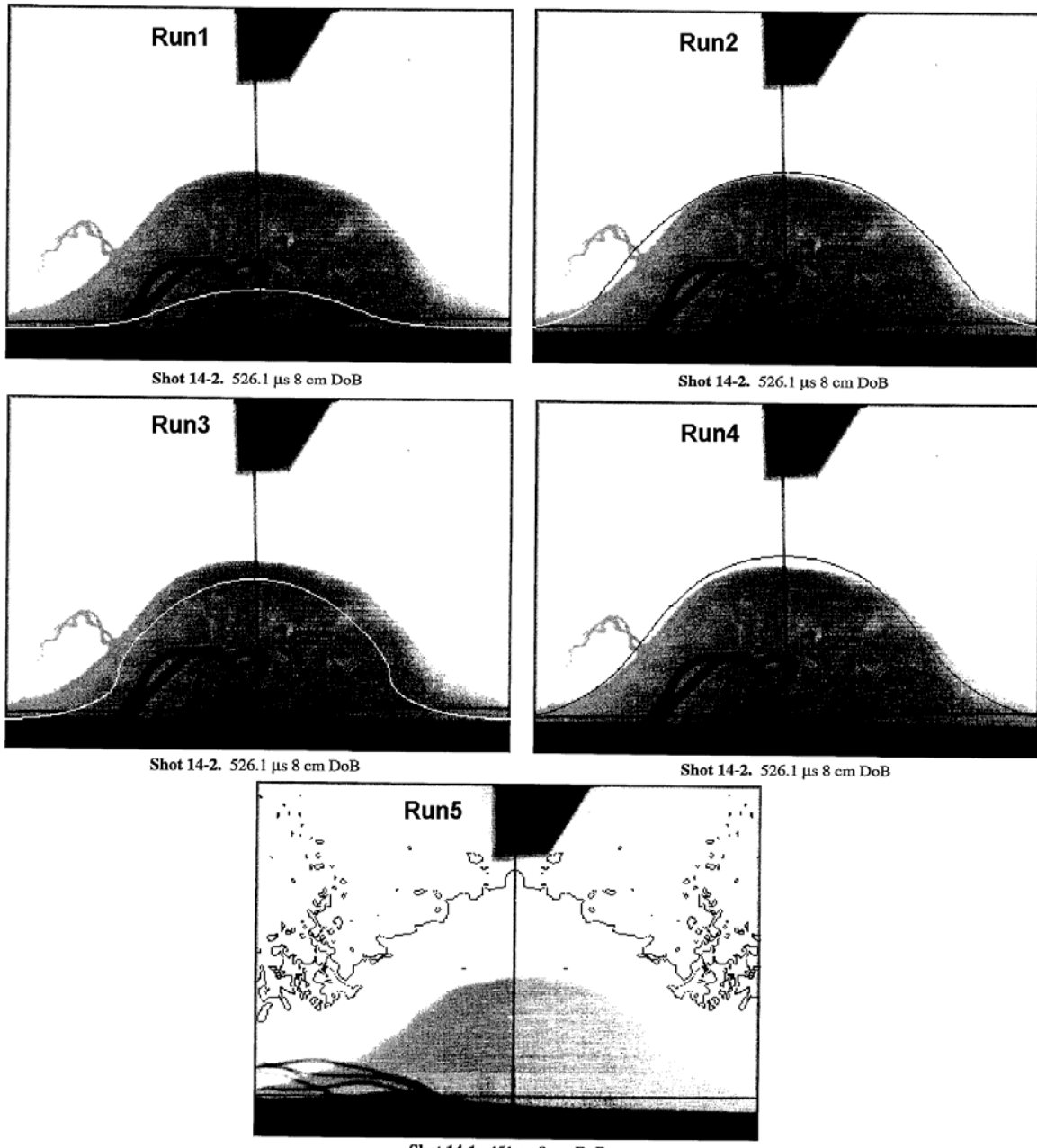


Figure 16. Comparison of experimental snapshots at late stage with the CTH results

The results of Run2 are drawn versus all available experimental snapshots in Fig. 17. It can be seen that the CTH calculation, employing the present implementation and selected parameters for the Run2 set-up, provides very good agreement with the experiment. It is interesting to note that all available model database calculations provide higher ejecta velocity than that observed in the camouflet blast experiments (with a fairly small excess, though, for the DRY SAND model). At the same time, CTH calculations (not described here) using the present implementation with even lower yield limits do not result in a further increase of the ejecta velocity.

## UNCLASSIFIED

DSTO-TR-2728

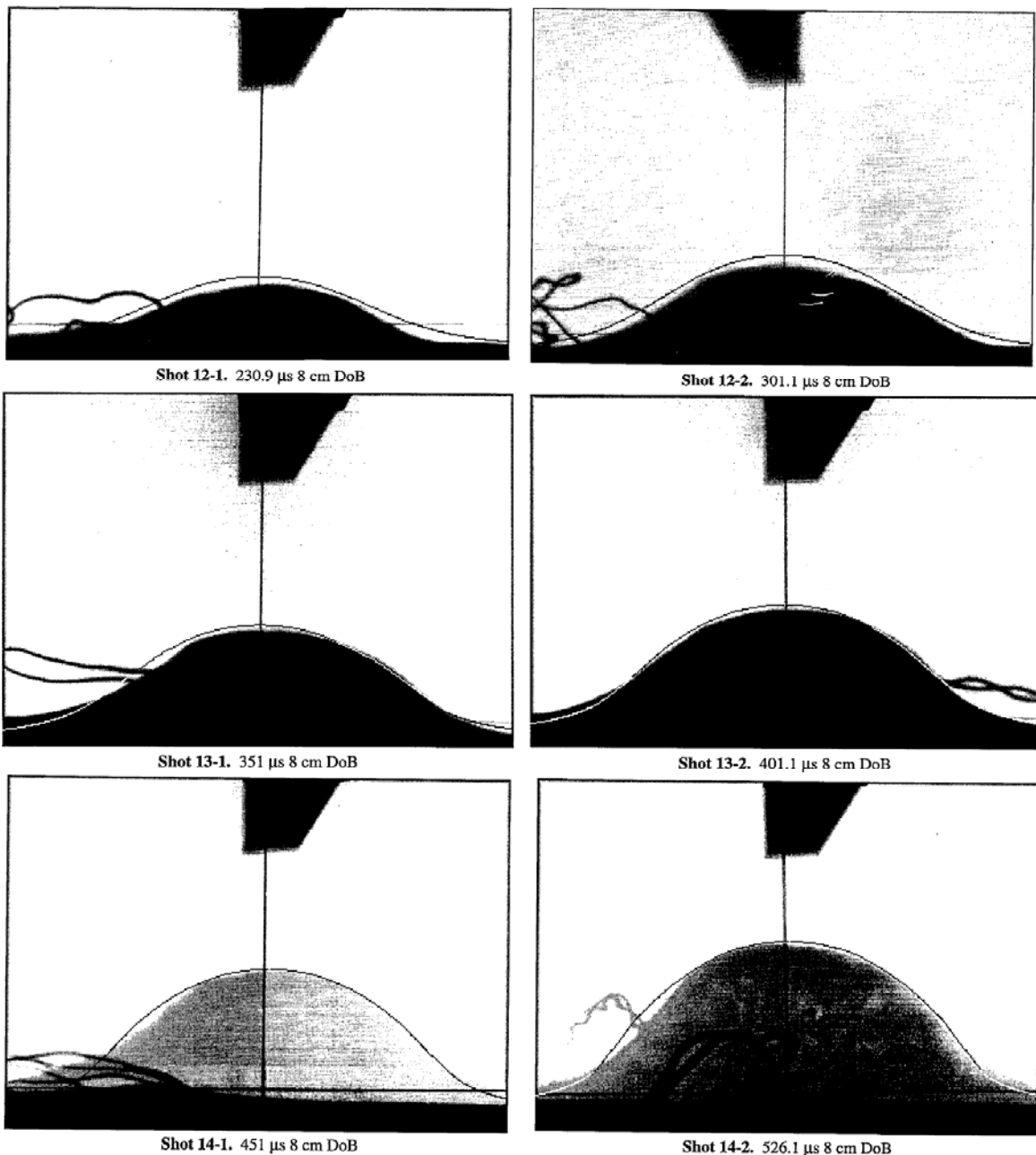


Figure 17. Comparison of the Run2 calculations with the experimental snapshots [12]

### 6.3 Calculations for Small Depth of Burial

When depth of burial decreases, the soil expansion regime changes from a confined underground blast (the camouflet blast) to soil ejection accompanied by an outburst of the detonation products through the soil surface. However, when the impact effect of the ejecta on a target is significant, the particles and detonation products are still relatively close to each other. Therefore, velocity equilibrium between products and particles can be assumed for this case, which allows us to describe the ejecta behaviour using the same models as in the

UNCLASSIFIED

previous subsection. The outburst regime realised at  $DOB = 3$  cm corresponds to the next characteristic mesh set-up selected for the second series of CTH calculations.

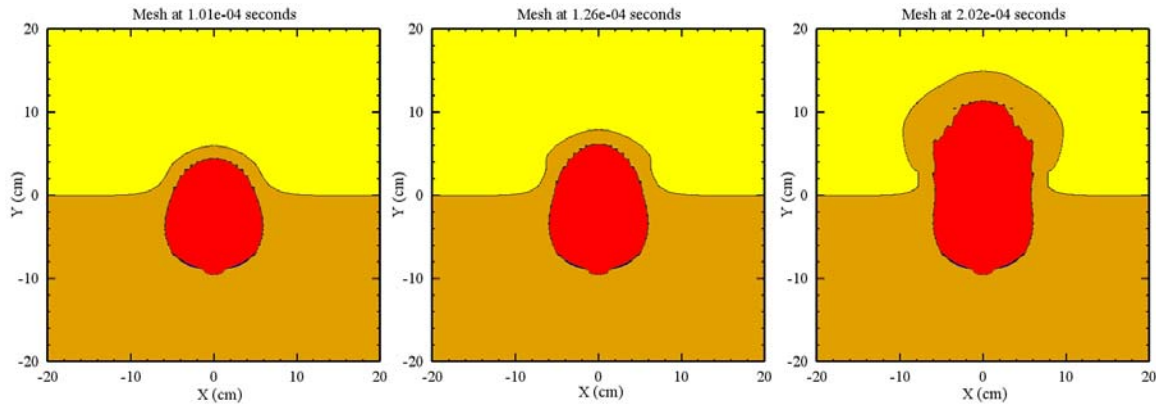


Figure 18. CTH calculation of the sand ejecta using the present model with parameters for Run6

Turning to the experimental data summarised in Table 2, the small DOB data at  $DOB = 3$  cm are grouped around the following three times, 101  $\mu$ sec, 126  $\mu$ sec and 201-202  $\mu$ sec. Therefore, plots for CTH calculations using the set-ups of Runs6-Run10 are only shown at these three times.

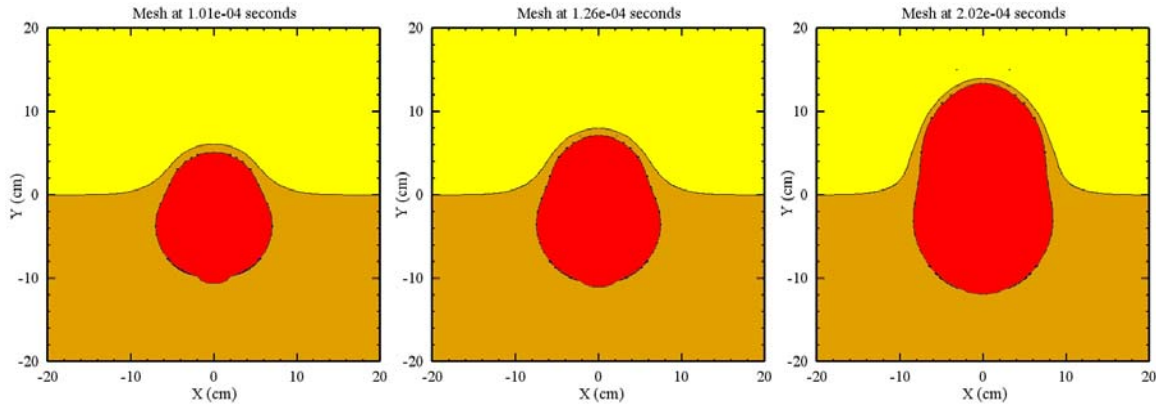


Figure 19. CTH calculation of the sand ejecta using the present model with parameters for Run7

As in the previous subsection, we start CTH analysis using the present implementation with the same three groups of the yield limit parameters. Numerical results for these parameters are obtained with the CTH runs, Run6, Run7, and Run8. Graphic representations of these results are shown in Figs. 18, 19, and 20 for Run6, Run7, and Run8, respectively.

## UNCLASSIFIED

DSTO-TR-2728

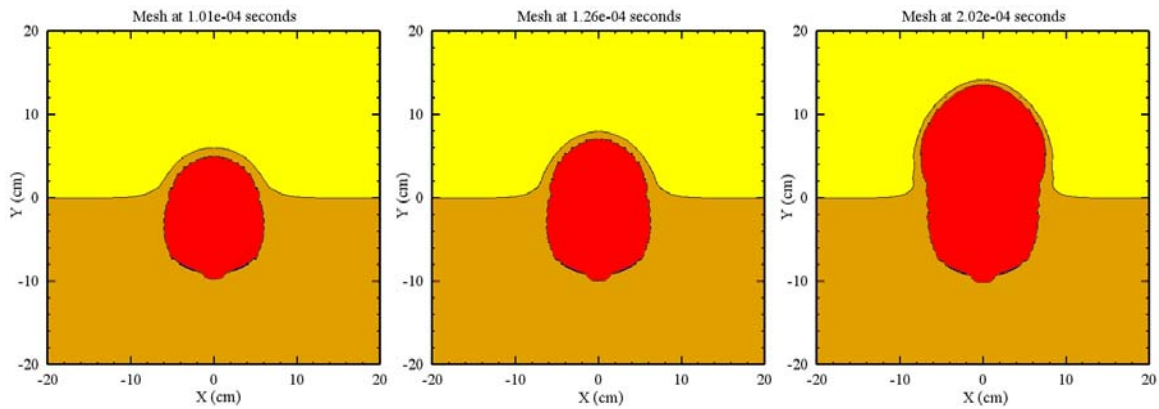


Figure 20. CTH calculation of the sand ejecta using the present model with parameters for Run8

Similarly to the previous calculation series, the drastically different ejecta shape among the results obtained with the CTH calculations employing the present implementation (Figs. 18-20) is observed in Fig. 18 for the case of the high yield limits at both compression and tension. It is interesting to note that the apparent ejecta shape appears to contradict the interpretation from Run1 where high strength at tension results in low bubble height. However, this apparent mesh contour for the porous material should be looked at in conjunction with the density plots, because the present model considers a two-phase mixture that may, for example, contain a prevailing volume of air.

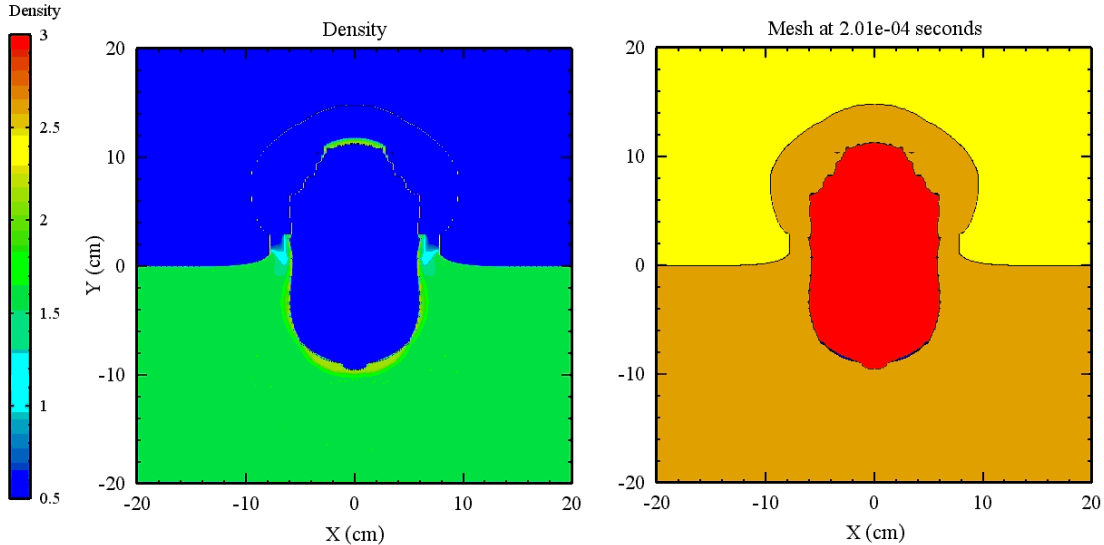


Figure 21. Density distribution inside the ejecta for Run6 calculation

Indeed, when plotting the density distribution for Run6 in Fig. 21 along with the material contours, it can be seen that the high-density (low-porosity) material is concentrated mainly at the lower boundary of the porous material and directly above the detonation products pushing the ejecta. Therefore, the actual height of the bubble carrying the prevailing mass is much smaller and it is adjacent to the upper boundary of the detonation products. At the same time, as seen from Figs. 19-20, the prevailing masses of the ejecta for Run7 and Run8 are concentrated in very narrow zones. Thus the ejecta contours for these two runs approximately correspond to the mesh contour of the ejecta drawn in Figs. 19 and 20.

## UNCLASSIFIED

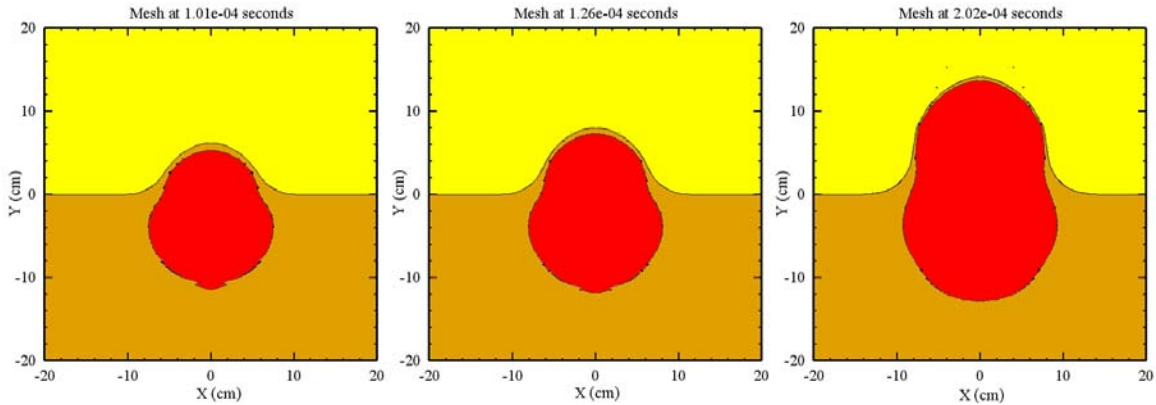


Figure 22. CTH calculation of the sand ejecta using the DRY SAND model (Run9)

The final two CTH calculations of the present series were conducted with the DRY SAND and P- $\lambda$  models from the CTH material database. The numerical results of these two runs are summarised in Fig. 22 (Run9) and Fig. 23 (Run10), respectively.

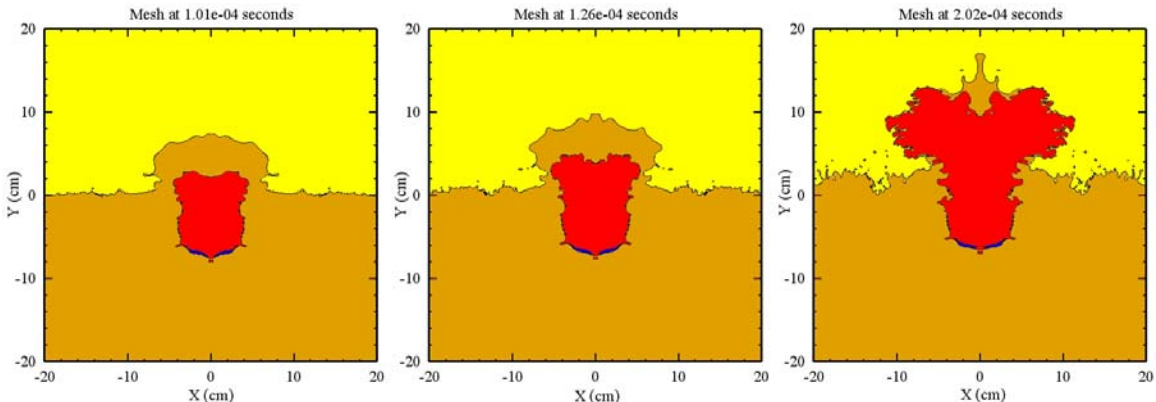


Figure 23. CTH calculation of the sand ejecta using the P- $\lambda$  model (Run10)

Similarly to Run7 and Run8, the calculation with the DRY SAND model, Run9, has the ejecta mass concentrated in a very narrow zone. Therefore, the ejecta contours in this case also correspond to the mesh boundary drawn in Fig. 22. The P- $\lambda$  model calculations shown in Fig. 23 result in an uncertain shape of ejecta and this case will be analysed below after comparison with the experiment.

Referring to the experimental data listed in Table 2, it can be seen that out of the 3 tests of this series (Shots 15, 16, and 17), the results of Shots 16 and 17 are more consistent to each other than the results of Shot 15. Indeed, the bubble height for snapshot 15-1 from Table 1 is close to that for snapshot 17-1, but at a significantly earlier time point. While, the bubble height for snapshot 15-2 essentially predominates the average bubble height at approximately the same time points from Shots 16 and 17.

## UNCLASSIFIED

DSTO-TR-2728

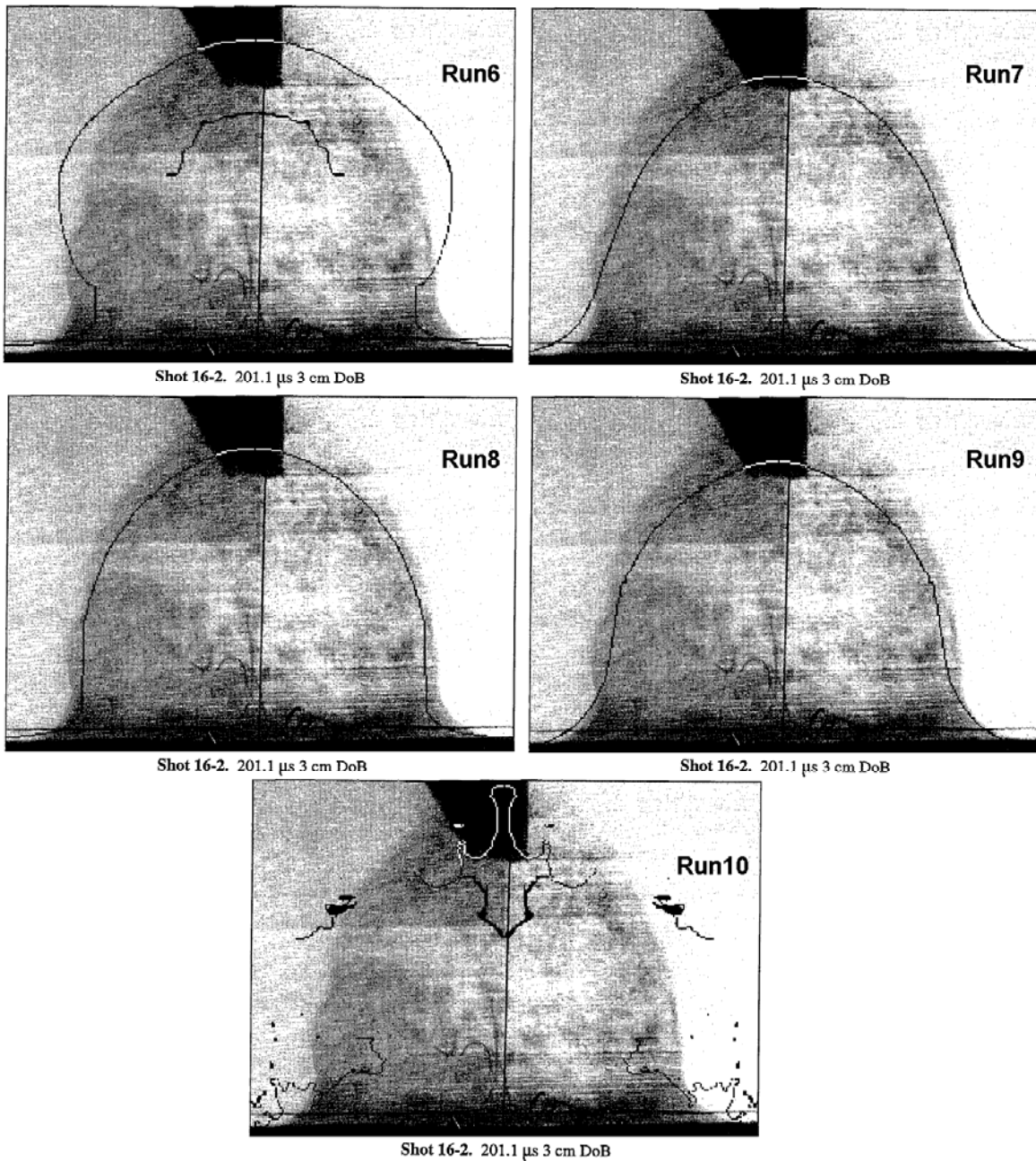


Figure 24. Comparison of experimental snapshots at late stage with the CTH results

Therefore, for comparison of the numerical results at a late stage of the soil expansion observed in the experiments we take the x-ray snapshot 16-2 that is quite similar to the snapshot 17-2. The comparison results are shown in Fig. 24 with run identifiers for the corresponding CTH calculation in each frame. From the comparison it might appear that the bubble height of Run6 agrees better with the experiment. However, as commented above in Fig. 21, the two-phase nature of the modelling should be remembered, whereby, the predominating mass bearing contour is drawn in the frame corresponding to Run6 together with the external ejecta contour. Comparison of this part of the ejecta with the experimental contour shows that the constraining effect of the high yield limits for the case of Run6 is also

UNCLASSIFIED

present for the small DOB calculations. Thus, similarly to the previous series of calculations, the last two runs with the low yield limits at tension (Run7 and Run8) produce more adequate results when compared with the experimental data.

Another candidate for a good description of the bubble height is the P- $\lambda$  model calculation of Run10. However, when referring to the density distribution of the P- $\lambda$  model calculation shown in Fig. 25, the major mass of the ejecta is again concentrated in the lowest part of the leading piece of the soil ejecta material similarly to the case of Run6. The corresponding mass bearing portion of the calculated ejecta plotted along with the external contour of the ejecta is shown in the last frame of the comparison graph in Fig. 24. Thus, the contour containing the major mass of the ejecta for this calculation describes the experiment in Fig. 24 more poorly than the similar contour for the case of Run6 criticised earlier. It could be argued that the fairly high yield limit value of 500 MPa selected for this calculation constrains the bubble height of the ejecta in the present case. However, when referring to the previous subsection calculations with this model (frame 5 in Fig. 16), it is seen that a reduction of the yield limit would result in an even larger discrepancy for that case shown in Fig. 16.

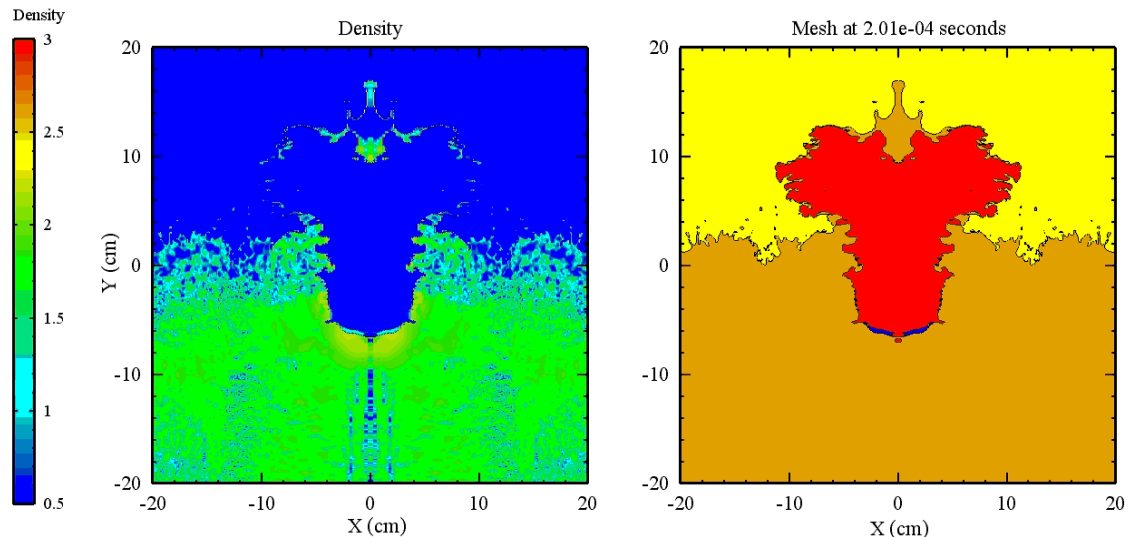


Figure 25. Density distribution inside the ejecta for Run10 calculation

Thus, from the comparison of the experimental snapshots with the CTH calculation results shown in Fig. 24, it is seen that Run8 results are reasonably close to the experimental bubble shape at a later stage of the soil expansion. When correlating the present model calculation plots with the yield limit input data from Table 1, it can be seen from Fig. 24 that a larger ejecta expansion in the middle section of the bell-shaped ejecta for small DOB is likely to be associated with a higher strength at compression.

Similarly to the large DOB case in the previous subsection, we summarise all available experimental snapshots for the small DOB with results of Run8 at approximately the same time points in Fig 26. It is seen that the CTH calculation using the present implementation with the Run8 parameters describes the experimental data (specifically, Shots 16 and 17) quite well. As commented earlier, possible inconsistency of Shot 15 should be kept in mind.

## UNCLASSIFIED

DSTO-TR-2728

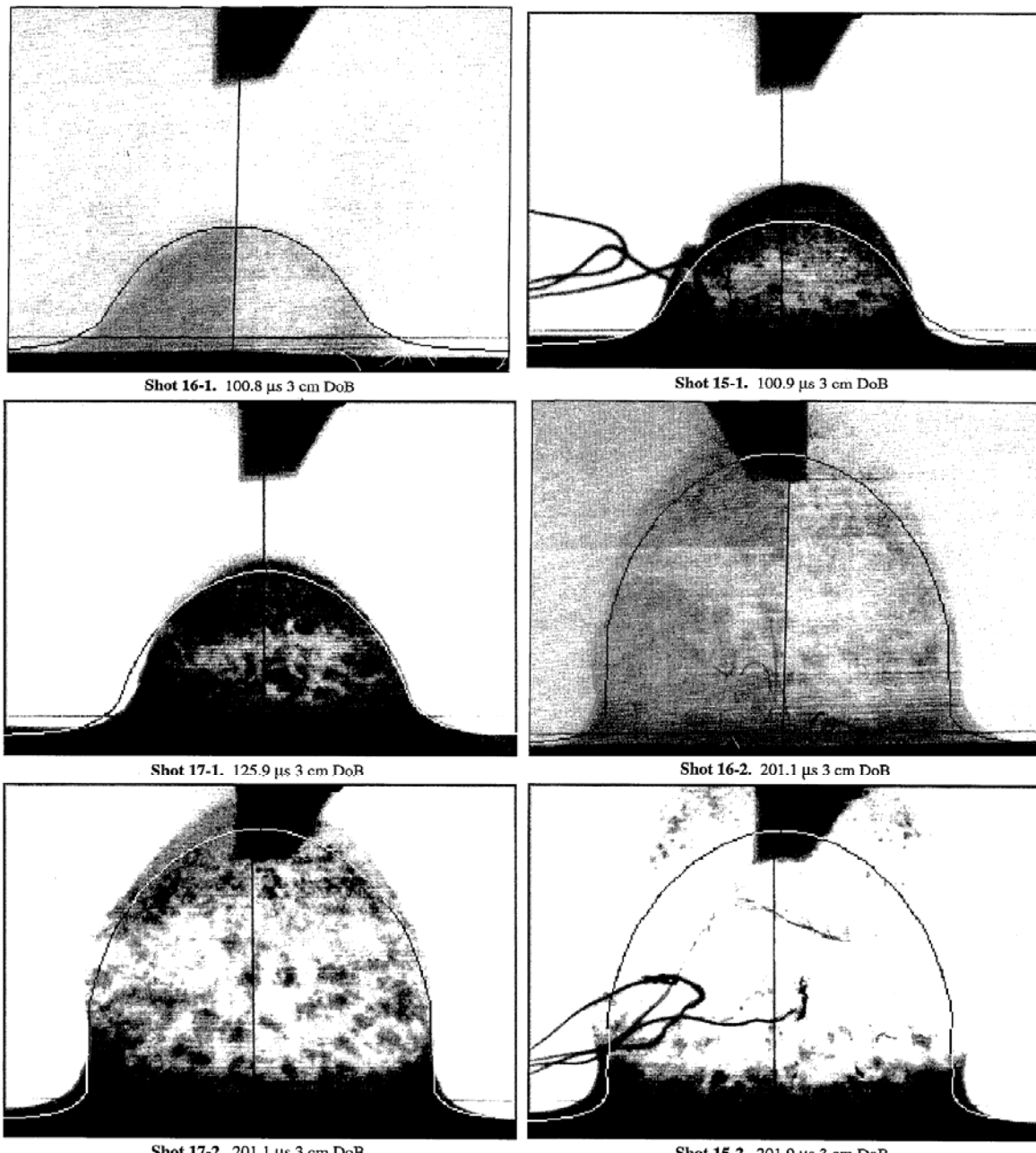


Figure 26. Comparison of the Run8 calculations with the experimental snapshots [12]

It should be noted that even good agreement of the ejecta shape with the experimentally observed contours does not guarantee a good prediction of the momentum transfer to a target. To illustrate this point, the numerical results of two runs for the small DOB at  $t = 50 \mu$ sec (one of the runs with the present model, Run6, and Run9 with the DRY SAND model) for mesh, density, pressure, and velocity magnitude are superimposed onto 4 single plots in Fig. 27. The left half of each graph corresponds to the calculation with the DRY SAND model and the right half represents the results calculated with the present implementation.

UNCLASSIFIED

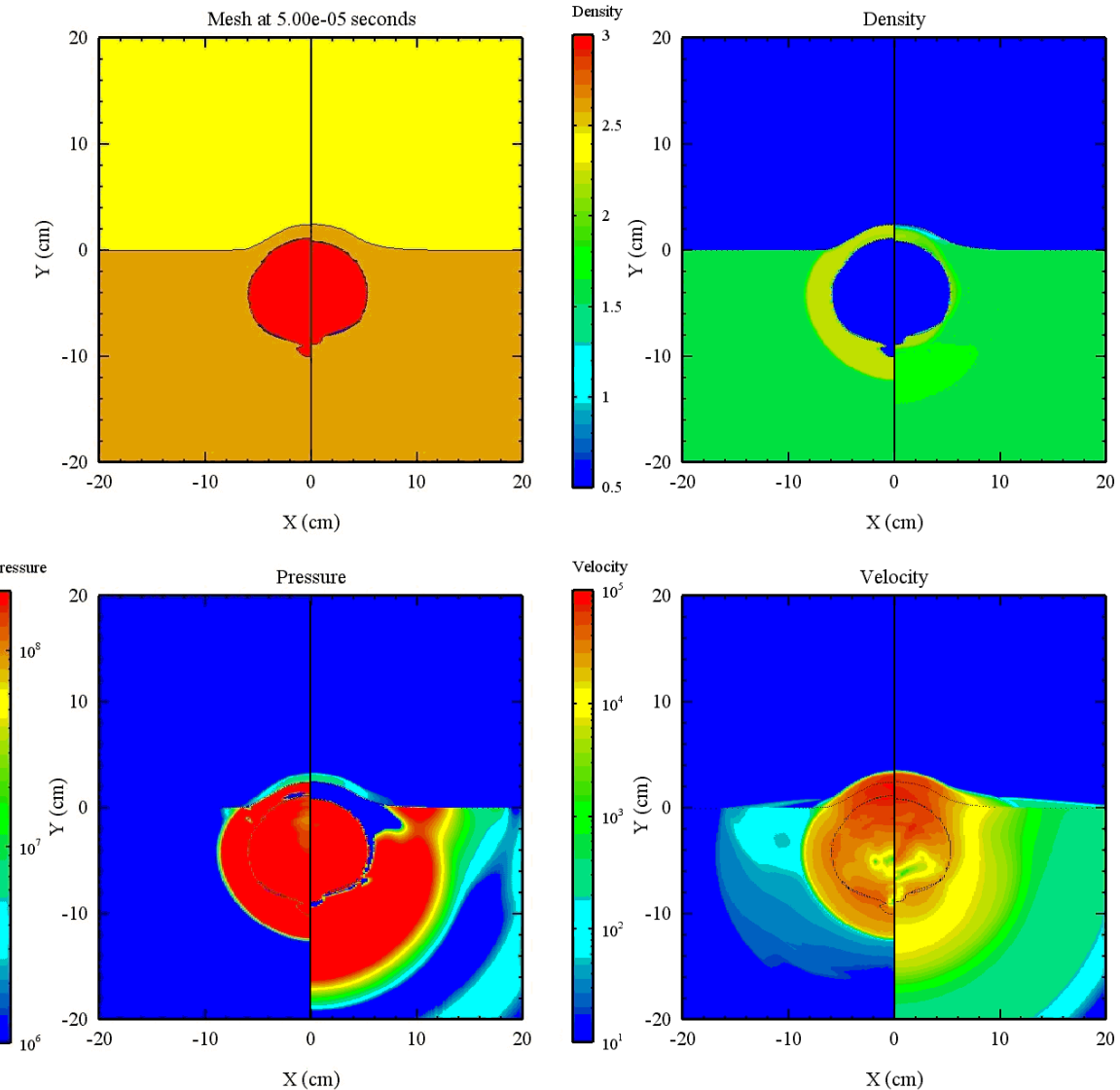


Figure 27. Comparison of the DRY SAND model results (the left half of the plots) with the present model implementation results (the right half of the plots) with DOB = 3 cm at  $t = 50 \mu\text{sec}$  (Run9 and Run6 results)

It can be seen that at times shown in the graph the velocities of ejecta are approximately the same from both the velocity fringes and contour positions. The contour shapes are quite similar at this moment of time for both cases, but the density distributions differ dramatically (the same point was also illustrated by the one-dimensional simulations of the previous section). The sand density is nearly constant through the ejecta thickness for the DRY SAND model with the SESAME EOS, whereas the material compaction in the present model is performed in a kinetic manner demonstrating a significant mass gradient through the ejecta thickness (as also observed in the one-dimensional calculations). Thus, the momentum transfer can be significantly overestimated with the tabulated SESAME approach. At the same time, model preference cannot be established before verification of the numerical results with experimentally measured through-thickness density distribution or with recorded momentum appropriately resolved in time has been conducted. Appropriately designed experiments

UNCLASSIFIED

DSTO-TR-2728

should allow measurement of the momentum sensitivity to target parameters or to record directly a pulse in the porous sample by a gauge.

## 7. Conclusions

As a further development of the basic CTH implementation capability established in DSTO earlier (see [5]), the present work describes another CTH implementation of a two-phase porous material model [4]. The implemented model is capable of describing the anomalous behaviour of highly porous materials, keeping the formalism consistent with that of the irreversible extended thermodynamics (e.g. [17]). The model is also capable of describing the phase transition effects and strain rate elasto-plastic effects.

The present implementation is consistent with the CTH user implementation interface [3, 19]. This means that 1) the implementation employs the mathematical model presented as the conservation laws with a set of constitutive equations evolving along the particle trajectory; and 2) the stress response is decoupled in volumetric (pressure) and deviatoric (shear stresses) responses. The implementation is realised in the present work for the case of porous materials and the implementation flowchart is briefly outlined in accordance with the code structure described in the available literature.

The model implementation has been verified for a highly porous silica material against the available Hugoniot data [11] and against calculations using an in-house code [4, 6, 7]. The CTH results correlate well with the calculations and with the anomalous behaviour of the material observed in the literature. Driven by the requirements of the counter-mine and counter-IED project, the literature data [12] on the explosion of a 100 g C4 charge buried under a layer of sand have been simulated with the present model. The CTH results demonstrate a good description of the experimental data by accurately following the soil ejecta shape.

Results of the present report have demonstrated that an advanced CTH implementation capability for multi-phase models has been established in DSTO. However, use of the implemented models concurrently and an extensive use of the extra variables in the model implementation will require even more intrusive implementation in the ERB part of the code along with the possibility of routine updating of extra implemented models in the EOS part of the code (this capability is currently available only in the EP part of the code). This access will also be critical when sharing implemented models within joint projects.

Addressing the accuracy of the description of the target response to the ejecta effects, further validation is necessary, which would allow one to evaluate the density and velocity distributions through the ejecta thickness and compare them with experiments. This can only be done by validation against specially designed experiments.

UNCLASSIFIED

## Acknowledgements

The author is grateful to Dr. David Crawford for supporting CTH in DSTO and for useful communications, to Dr. Gene Hertel for useful comments, and to Drs. Shane Schumacher and Bob Schmitt of SNL for useful communication on the implementation issues in the Eulerian modules of the code.

## References

1. Resnyansky A.D., Bourne N.K., Millett J.C.F., and Brown E.N., Constitutive modeling of shock response of polytetrafluoroethylene, *J. Appl. Physics*, 2011, v. 110, n. 3, pp. 033530-15.
2. Hallquist, J.O., Stillman D.W., and Lin T-L., "LS-DYNA3D User's Manual", Livermore Software Technology Corporation, Livermore, CA, 1994.
3. Bell R.L., Baer M.R., Brannon R.M., Crawford D.A., Elrick M.G., Hertel E.S. Jr., Schmitt R.G., Silling S.A., and Taylor P.A., "CTH user's manual and input instructions version 7.1", Sandia National Laboratories, Albuquerque, NM, 2006
4. Resnyansky A.D., Constitutive modeling of shock response of phase-transforming and porous materials with strength, *J. of Appl. Physics*, 2010, v. 108, n. 8, pp. 083534-13.
5. Resnyansky A.D., Thermodynamically Consistent Decoupled Shear-Volumetric Strain Model and CTH Implementation, Report DSTO-TR-2299, DSTO, Edinburgh, Australia, 2009, 30 pp.
6. Resnyansky A.D. and Bourne N.K., Shock-wave compression of a porous material, *J. Appl. Physics*, 2004, v. 95, n. 4, pp. 1760 - 1769.
7. Resnyansky A.D., Constitutive Modelling of Hugoniot for a Highly Porous Material, *J. Appl. Physics*, 2008, v. 104, n. 9, pp. 093511-14.
8. McGlaun J.M., Thompson S.L., and Elrick M.G., CTH: A three-dimensional shock wave physics code, *Int. J. Impact Eng.*, 1990, v. 10, n. 1-4, 1990, pp. 351-360.
9. Fahrenhold E.P. and Yew C.H., Hydrocode simulation of hypervelocity impact fragmentation, *Int. J. Impact Eng.*, 1995, v. 17, n. 1-3, pp. 303-310.
10. Dey T.N., An effective model for dynamic finite difference calculations, Los Alamos National Laboratory Report LA-13093-MS, UC-703, Los Alamos, NM, 1996.
11. Simakov G.V. and Trunin R.F., Shockwave Compression of Ultraporous Silica, *Izv. Earth Physics*, 1990, v. 26(11), pp. 952-956.
12. Bergeron D., Walker R., and Coffey C., Detonation of 100-Gram Anti-Personnel Mine Surrogate Charges In Sand - A Test Case For Computer Code Validation, Report DRES-668, DRES, Ralston, Alberta, Canada, 1998, 206 pp.
13. Resnyansky A.D., DYNA-modelling of the high-velocity impact problems with a split-element algorithm, *Int. J. Impact Eng.*, 2002, v. 27, n. 7, pp. 709-727.
14. Romenski E., Resnyansky A.D., and Toro E.F., Conservative hyperbolic formulation for compressible two-phase flow with different phase pressures and temperatures, *Quart. Appl. Math.*, 2007, v. 65, n. 2, pp. 259-279.
15. Dorovskii V.N., Iskol'dskii A.M., and Romenskii E.I., Dynamics of impulsive metal heating by a current and electrical explosion of conductors, *J. Appl. Mech. and Techn. Phys.*, 1983, v. 24, n. 4, pp. 454-467.

## UNCLASSIFIED

DSTO-TR-2728

16. Merzhievskii L. A. and Shamonin S. A., Construction of the time dependence of the relaxation of tangential stresses on the state parameters of a medium, *J. Appl. Mech. and Techn. Phys.*, 1980, v. 21, n. 5, pp. 716-724.
17. Godunov S. K. and Romenskii E. I., "Elements of Continuum Mechanics and Conservation Laws", Kluwer, New York, 2003.
18. Martin B.E., Chen W., Song B., and Akers S.A., Moisture effects on the high strain-rate behavior of sand, *Mechanics of Materials*, 2009, v. 41, pp. 786-798.
19. Brannon, R.M. and Wong, M.K., MIG version 0.0 model interface guidelines: Rules to accelerate installation of numerical models into any compliant parent code, Sandia National Laboratories Report SAND96-2000, UC-405, Unlimited Release, Albuquerque, NM, 1996.
20. Benson D.J., The Numerical Simulation of the Dynamic Compaction of Powders, In: "High-Pressure Shock Compression of Solids IV: Response of Highly Porous Solids to Shock Loading", Davison L.W., Horie Y., and Shahinpoor M., Eds., Springer-Verlag, 1997, pp. 233-255.
21. Bell R.L., An Isotropic Material Remap Scheme for Eulerian Codes, In: Second Int. Conf. on Cybernetics and Information Technologies, Systems and Applications (CITSA 2005) jointly with the 11th Int. Conf. on Information Systems Analysis and Synthesis (ISAS 2005), July 14-17, 2005 - Orlando, Florida, USA.
22. Hertel E.S. Jr. and Kerley G.I., CTH EOS Package: Introductory Tutorial, Sandia National Laboratories Report SAND98-0945, UC-705, Albuquerque, NM, 1998.
23. Lyzenga G.A., Ahrens T.J. and Mitchell A.C., Shock Temperatures of SiO<sub>2</sub> and Their Geophysical Implications, *J. Geophys. Res.*, 1983, v. 88, n. B3, pp. 2431-2444.
24. Peselnick L., Meister R., and Wilson W.H., Pressure derivatives of elastic moduli of fused quartz to 10 kb, *J. Phys. & Chem. of Solids*, 1967, v. 28, n. 4, pp. 635-639.
25. Marsh S.P. (Ed.), "LASL Shock Hugoniot Data", University of California Press, Berkley and Los Angeles, California, 1980.
26. Boehler R., Skoropanov A., O'Mara D., and Kennedy G.C., Grüneisen parameter of quartz, quartzite, and fluorite at high pressure, *J. Geophys. Res.*, 1979, v. 84, n. B7, pp. 3527-3531.
27. Ai H.-A. and Ahrens T.J., Dynamic tensile strength of terrestrial rocks and application to impact cratering, 2004, *Meteoritics & Planetary Sci.*, v. 39, n. 2, pp. 233-246.
28. Asprone D., Cadoni E., Prota A., and Manfredi G., Dynamic behavior of a Mediterranean natural stone under tensile loading, *Int. J. Rock Mech. Mining Sci.*, 2009, v. 46, n.3, pp. 514- 520.
29. Godunov S.K., Zabrodin A.V., Ivanov M.Ya., Kraiko A.N., and Prokopov G.P., "Numerical Solution of Multi-Dimensional Problems of Gas Dynamics", Nauka Press, Moscow, 1976 (French transl: "Résolution Numérique des Problèmes Multidimensionnels de la Dynamique des Gaz", Mir, Moscow, 1979).
30. Johnson J.D., The SESAME database, Report LA-UR-94-1451, LANL, Los Alamos, New Mexico, 1994, 44 pp.
31. Grady D.E. and Winfree N.A., A computational model for polyurethane foam, In: "Fundamental Issues and Applications of Shock-Wave and High-Strain-Rate Phenomena", Staudhammer K.P., Murr L.E., and Meyers M.A., Eds., 2001, pp. 485-491.

UNCLASSIFIED

<b>DEFENCE SCIENCE AND TECHNOLOGY ORGANISATION DOCUMENT CONTROL DATA</b>		1. PRIVACY MARKING/CAVEAT (OF DOCUMENT)		
2. TITLE  CTH Implementation of a Two-Phase Material Model With Strength: Application to Porous Materials		3. SECURITY CLASSIFICATION (FOR UNCLASSIFIED REPORTS THAT ARE LIMITED RELEASE USE (L) NEXT TO DOCUMENT CLASSIFICATION)  Document (U) Title (U) Abstract (U)		
4. AUTHOR(S)  A.D. Resnyansky		5. CORPORATE AUTHOR  DSTO Defence Science and Technology Organisation PO Box 1500 Edinburgh South Australia 5111 Australia		
6a. DSTO NUMBER DSTO-TR-2728	6b. AR NUMBER AR-015-382	6c. TYPE OF REPORT Technical Report	7. DOCUMENT DATE July 2012	
8. FILE NUMBER 2012/1104378/1	9. TASK NUMBER CDF 07/331	10. TASK SPONSOR VCDF	11. NO. OF PAGES 44	12. NO. OF REFERENCES 31
DSTO Publications Repository  <a href="http://dspace.dsto.defence.gov.au/dspace/">http://dspace.dsto.defence.gov.au/dspace/</a>		14. RELEASE AUTHORITY  Chief, Weapons Systems Division		
15. SECONDARY RELEASE STATEMENT OF THIS DOCUMENT				
<i>Approved for public release</i>				
OVERSEAS ENQUIRIES OUTSIDE STATED LIMITATIONS SHOULD BE REFERRED THROUGH DOCUMENT EXCHANGE, PO BOX 1500, EDINBURGH, SA 5111				
16. DELIBERATE ANNOUNCEMENT				
No Limitations				
17. CITATION IN OTHER DOCUMENTS		Yes		
18. DSTO RESEARCH LIBRARY THESAURUS				
Material model; Multi-phase flows; Hydrocodes; Shock-wave response; Porous material				
19. ABSTRACT  A material model accounting for strength developed earlier for two-phase materials is implemented in the CTH hydrocode. The strain response to load in the model is decoupled into shear and volumetric contributions in order to satisfy the model implementation requirements for CTH. Multi-phase description is realised via constitutive equations complementing the conservation laws for a material represented as a mixture of several phases. Such a formulation agrees well with the CTH code structure and is suitable for conventional user implementation. The implementation has been applied to a generic material representing sand at various porosities. The constitutive equations and equations of state have been fitted in order to describe literature data. Numerical illustrations in the report demonstrate agreement of the calculation results with the anomalous behaviour observed in the literature for a highly porous sand at shock compression and a good description of the experiments available in the literature on the explosion of a sand-buried charge.				